Summer 7-29-2020

Characterizing the Empirical Drivers of the Carbon Fluxes of an Inland Salt Marsh

Veronica Davies
SUNY College of Environmental Science and Forestry, vldavies@syr.edu

CHARACTERIZING THE EMPIRICAL DRIVERS OF THE CARBON FLUXES OF AN INLAND SALT MARSH

by

Veronica Davies

A thesis submitted in partial fulfillment
of the requirements for the Master of Science Degree
State University of New York
College of Environmental Science and Forestry
Syracuse, New York
July 2020

Graduate Program in Environmental Resources Engineering

Approved by:
Timothy Morin, Major Professor
Stephen Stehman, Chair, Examining Committee
Lindi Quackenbush, Department Chair
S. Scott Shannon, Dean, The Graduate School

Acknowledgments

I would like to thank my family and friends for their encouragement throughout this process. This would not have been possible without the constant support from my parents, brother, friends, and my camping backpack. I will cherish the memories I made with them on the mountains, slopes, and nearby the lakes. The last two years have opened my eyes to the natural beauties of New York, gave me a new outlook on terrestrial systems, and introduced me to the most amazing people, the SUNY ESF cohort.

I would like to thank SUNY ESF, the ERE department, and, more specifically, Timothy Morin for affording me this opportunity to attend graduate school. I was the first graduate student to join Tim's lab, and with that came endless opportunities for growth. From Tim's example, I am leaving SUNY ESF with the ability to think on my feet, share scientific knowledge with a sense of humor, and to lead with empathy.

Table of Contents

List of Abbreviations and Acronyms

AIC	Akaike Information Criterion
ANN	Artificial Neural Network
BIC	Bayesian Information Criteria
C	Carbon
°C	Celsius
CH_4	Methane
CO_2	Carbon Dioxide
CS	Campbell Scientific
DO	Dissolved Oxygen
G-causality	Granger Causality
GPP	Gross Primary Production
H_2O	Water
ha	Hectare
hPa	Hectopascal
IPCC	Intergovernmental Panel On Climate Change
L	Obukhov Atmospheric Stability Length
LE	Latent Heat Flux
LI	Licor
m	Meter
mm	Millimeter
mol	Mole
N	Nitrogen
NDVI	Normalized Difference Vegetation Index
$NDVI_{fwt}$	Normalized Difference Vegetation Index Footprint Weighted Total
NEE	Net Ecosystem Exchange
Net_{Rad}	Net Radiation
P_a	Atmospheric Pressure
PAR	Photosynthetically Available Radiation
PPT_T	Precipitation Total
R_a	Autotrophic Respiration
R_e	Ecosystem Respiration
R_h	Heterotrophic Respiration
s	Second
SSB	Solvay Sediment Basins
SW	South West
T_{Air}	Air Temperature
T_{Soil}	Soil Temperature
u*	Friction Velocity

v'v'	Crosswind Variation
VPD	Vapor Pressure Deficit
W	Watts
$Wind_{dir}$	Wind Direction
$Wind_{speed}$	Wind Speed
WPL	Webb, Pearman And Leuning
μ	Micro-

List of Tables

List of Figures

Abstract

V.L. Davies. Characterizing the empirical drivers of the carbon fluxes of an inland salt marsh. 69 Pages, 8 Tables, 16 Figures, 2020. APA Style Guide used.

Wetlands promote carbon sequestration through saturated, anoxic soils. However, the persistent presence of water results in reduce conditions, which promotes methane (CH_4) production. The climatological variables responsible for the source/sink behavior are still unclear. This study quantifies temporal changes in the empirical drivers of the carbon fluxes of a constructed inland salt marsh in Camillus, New York. The mean CH_4 (0.328 $\mu mol \cdot m^{-2} \cdot s^{-1}$) and carbon dioxide ($CO_2$) (0.195 $\mu mol \cdot m^{-2} \cdot s^{-1}$) emissions from June 27, 2019 to November 11, 2019 show the site's slight carbon source behavior. Latent heat flux had the strongest relationship with CH_4 and gross primary production (GPP), while air temperature best explained ecosystem respiration (R_e). The lag responses of R_e (3-hours) and CH_4 (5-hours) from air temperature are likely attributed to the lag response between the air and soil temperature. Whereas the lag response of GPP (1-hour), R_e (2-hours), and CH_4 (1-day) from rainfall events are likely a reflection of an increase in dissolved oxygen and soil moisture content.

Keywords: methane, ecosystem respiration, gross primary production, net ecosystem exchange, wetland, eddy covariance, lag response, normalized difference vegetation index

V.L. Davies
Candidate for the degree of Master of Science, July 2020
Timothy H Morin, Ph.D
Department of Environmental Resources Engineering
State University of New York College of Environmental Sciences and Forestry
Syracuse New York

Chapter 1: Introduction

Wetlands offer a variety of ecosystem services, including biodiversity support, water quality improvement, flood abatement, and carbon management (Zedler and Kercher, 2005). The Intergovernmental Panel on Climate Change (IPCC; Intergovernmental Panel on Climate Change and Edenhofer, 2014) lists wetlands as a potential mitigation strategy to combat climate change through the sequestration of carbon across soil pools, peat formation, sediment decomposition, and plant biomass (Bridgham et al., 2006). It is estimated that wetland soils contain 20-30% of the total storage of carbon in the earth's soils (Bridgham et al., 2006; Roulet, 2000), the equivalent of 75% of the earth's total atmospheric carbon (Piao et al., 2009). However, wetlands also emit 30% of the global methane (CH_4) emissions, which has 28 times the global warming potential (GWP) of carbon dioxide (CO_2) when considered over a 100-year time horizon (Edenhofer, 2015). Thus, wetlands occupy a unique climatological niche, where they can be carbon sinks but global warming sources. The ecological drivers responsible for the source/sink behavior of wetlands are still not clear; however, it is essential to understand the climatological variables that drive engineered wetlands' CO_2 and CH_4 fluxes in order to optimize their carbon and warming budgets.

Over the last two decades, scientist conducted many observational studies (Baldocchi et al., 2001; Inglett et al., 2012; Kim et al., 1998; Morin et al., 2014a; Rey-Sanchez et al., 2018; Rinne et al., 2007, 2018) to measure the ecosystem-level greenhouse gas vertical fluxes of wetlands using the eddy covariance technique. The eddy covariance method provides temporally continuous and spatially integrated flux measurements of an ecosystem by measuring the

turbulent diffusion of gases at a set height above the atmosphere-ecosystem interface (Baldocchi, 2003; Schmid, 1994). The integration of fluxes originating from a large area referred to as the tower footprint dampens the sampling bias due to spatially heterogeneous fluxes, which provides an accurate estimation of the site-level total fluxes. Efforts have been made to use observed responses to create and validate empirical models to examine the influence of any predictor variable on the final observed fluxes. Empirical models for CO_2 and CH_4 fluxes may incorporate a wide host of environmental variables (e.g., meteorological data, soil characteristics, types and diversity of plants, etc.), which can provide insight into the underlying statistical relationships from multiple data sets simultaneously (Morin et al., 2014b). For example, climatological variables such as T_{Air} and PPT_T affect the carbon behavior of wetlands based on their influence on soil temperature and the water table level, which directly influence above- and below-ground carbon fluxes.

Despite these efforts, discrepancies between estimated carbon responses among wetland types and locations suggest a need for more ecosystem-level efforts to explain temporal (across seasons and days) and spatial variation and for model validation (Kirschke et al., 2013). Furthermore, environmental conditions may drive future CO_2 and CH_4 emissions, potentially inducing a phase lag between the two signals (Kim et al., 1998). Lag response due to weather events cause delayed effects due to changes in the water table level, altered vegetation activity, and atmospheric stability and mixing. Continuous measurement of the fluxes permits temporal analyses and provides insight into the temporal dynamics of the climatological variables and the ecosystem carbon exchange.

Fluxes also vary spatially due in part to the spatial heterogeneity of above- and below-ground conditions, including the presence or absence of standing water, the vigor of plants, or the depth of labile carbon availability (Sha et al., 2011). The integration of these environmental variables into the eddy-covariance tower footprint metrics provides insight into spatial drivers. Recent developments in remote-sensing measurements allow for spatial variation in plant productivity in the form of the normalized difference vegetation index (NDVI). The integration of NDVI can provide understanding to gross primary production (GPP), CH_4, and ecosystem respiration (R_e) drivers, and CH_4 transport through the vegetation (Boon, 2000). Ultimately, NDVI and temporal changes in climatological variables may help offer insight into site-specific responses and model validation.

The broad goal of this study is to characterize the empirical drivers of the carbon fluxes of a constructed inland salt marsh in Camillus, New York. To accomplish this, we measured and modeled the CH_4, GPP, and R_e fluxes from the constructed inland salt marsh using the eddy covariance method from June 27, 2019 to November 11, 2019. We set three research objectives:

1) Determine temporal changes in the statistical relationships between the carbon fluxes and the climatological variables (air temperature, precipitation, vapor pressure density, net radiation, wind speed, wind direction, atmospheric pressure, heat flux, and low friction velocity) and vegetative distribution (NDVI footprint weighted total) using an empirical model.
2) Determine the frequency response of the ecosystem's carbon exchange (CH_4, GPP, R_e) to precipitation events and shifts in atmospheric temperature during the growing season.

3) Evaluate the spatial influence of a heterogeneous plant community from an individual NDVI event on site-level integrated carbon fluxes.

Chapter 2: Methods

2.1 Site Description

The Solvay inland salt marsh (Figure 1) is a 2.1 hectare (ha) wetland built on top of a sediment basin located in Camillus, New York. Historically, the Solvay Sediment Basins 12-15 (SSB), was filled with Solvay waste, composed of calcium carbonate and other salts of calcium, magnesium, and sodium, from a local soda ash production facility (mid-1900's -1986) (Hewlett, 1956; Mirck and Volk, 2010). The original filling of the SSB left a depression in the center of sediment basin 14 (43°04'10" N, 76°15'45" W, 140 m altitude), which accumulated drainage from the surrounding SSB, leaving the depression with alkaline, infertile soil with a pH and total Nitrogen (N) approximately 8.5 and 0.5%, respectively (Eallonardo, 2010). In 2008, through a collaboration between the State University of New York College of Environmental Science and Forestry, Honeywell International, and O'Brien & Gere Engineers, the seasonally flooded depression was converted to an inland salt marsh and the surrounding SSB were enclosed in a willow-based evapotranspiration cover system (New York State Department of Environmental Conservation, 2010) to reduce leachate. The decision to select inland salt marsh as the restoration target was decided due to the extreme soil conditions caused by the high alkalinity, low total N (Eallonardo, 2010), and volumetric water content of 70% at saturation (Hewlett, 1956; Mirck and Volk, 2010).

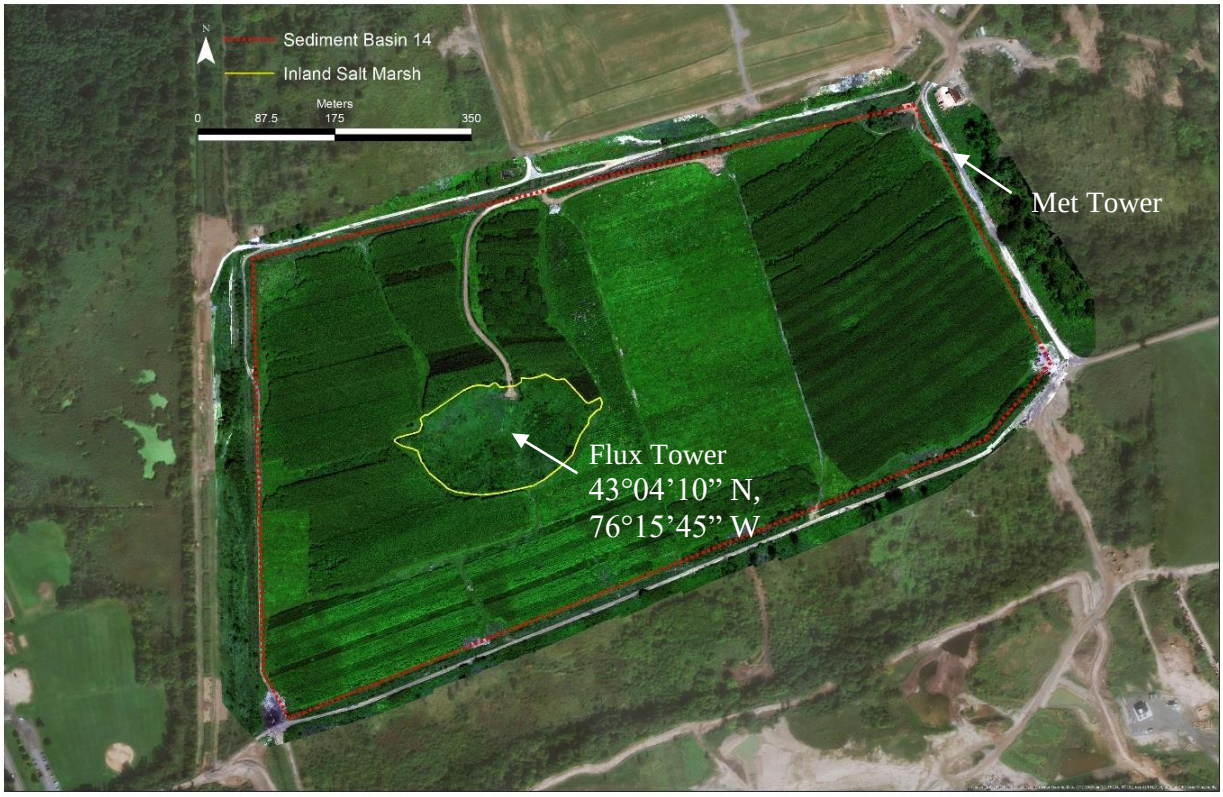

Figure 1. Aerial representation of the inland salt marsh and willow beds on sediment basin 14. The flux tower captured the carbon fluxes, latent heat flux (LE), wind speed ($wind_{speed}$), wind direction ($wind_{dir}$), and friction velocity (u*) from June 27, 2019 until November 11, 2019 (observational period). The meteorological station collected air temperature (T_{Air}), precipitation total (PPT_T), net radiation (net_{Rad}), atmospheric pressure (P_a), and vapor pressure deficit (VPD) through the observational period.

The vegetation of the inland salt marsh is a combination of alvar grassland, inland salt marsh, Great Lakes dune, and marl fen plant communities which were introduced to the site from 2008 to 2010 (Eallonardo, 2010). Data collected from 2008 to 2013 demonstrated that vegetation development was rapid, with percent cover increasing from nearly 0% to 100% in six years. Herbaceous plant species that are 1 - 2 m tall dominate the site, with over 100% areal coverage.

The growing season typically lasts from the end of April through mid-October. The mean annual air temperature (T_{Air}) is 9°C (1989-2019) and the mean annual precipitation is 977 mm (1989-2019) (Binghamton, NY Weather Forecast Office, 2020).

2.2 Data Collection

We constructed the eddy-covariance tower on June 27, 2019 and ran continuously through November 11, 2019. The equipment on the tower includes two Infrared Gas Analyzers (IRGAs): a LI-7500RS (LI-COR Biosciences, Lincoln NE) for CO_2 and H_2O, and a LI-7700 (LI-COR Biosciences, Lincoln NE) for CH_4, and a CSAT3B sonic anemometer (Campbell Scientific, Inc. Logan, UT). The air pressure, three-dimensional wind velocities, and CO_2, CH_4, and H_2O concentrations were measured at 10 Hz and recorded on a CR3000 datalogger (Campbell Scientific, Inc. Logan, UT). The data were then transmitted from the tower via FM radio (RF451, Campbell Scientific, Inc. Logan, UT) to a nearby computer to be processed into 30-minute block averages using MATLAB (version R2018a, MathWorks, Natick, MA) using methods described originally in Morin et al., (2014a). Additional averaged hourly meteorological observations were recorded by a nearby meteorological tower (Figure 1), including T_{Air}, vapor pressure deficit (VPD), net radiation (net_{Rad}), atmospheric pressure (P_a), total rainfall (PPT_T), wind speed ($wind_{speed}$), and wind direction ($wind_{dir}$) throughout the observational period.

A DJI Matrice 100 drone (elevation 120 m) flew over the wetland on August 1, 2019 to capture multispectral data (blue, green, red, red edge, near-IR spectral bands) using a RedEdge-M multispectral camera (MicaSense, Inc., Seattle, WA) with an 80% front and side overlap and 4.2 cm^2 pixel resolution. The 5-band reflectance orthomosaic was processed using Pix4D mapper

photogrammetry software, including MicaSense supplied calibration targets, which were factored into the data from the onboard down-welling light sensor. The NDVI map was calculated using the red and near-infrared bands from the reflectance orthomosaic in ESRI ArcMap (Esri, Redlands, CA) and converted to a 1 m^2 pixel resolution.

2.3 Tower Configuration

Based on theory and practice, the tower's placement and design are determined to limit the systematic biases caused by flow distortions to best capture the climatological variables and processes from a heterogeneous environment. To do this, the tower's location, height, and orientation were all considered. Before tower placement, we estimated the footprint size using historical wind data gathered at the meteorological station (Figure 1). We used those data to determine the location and height of the tower, where the setup would have a relatively homogeneous topography within the fetch for all wind directions. The location was near the center of the wetland (Figure 1) downwind of the most spatially homogeneous portion of the wetland and far from surrounding trees and depressions in the wetland soils that could introduce irregular vertical wind conditions. This placement reduced wind streamline distortion caused by changes in the wind displacement height from varying vegetation within the tower's footprint.

We vertically positioned the sonic anemometer and the IRGAs by keeping in mind the following two considerations: 1) the instruments must be at least 1.5 times the vegetation height to be in the well-mixed surface layer and 2) the measurement height determines the fetch length of the tower, with a taller tower incorporating a larger area into each measurement. Prior to installation, we measured the height of the dead vegetation to determine the minimum height needed and

estimated the maximum height required from a preliminary footprint analysis. We mounted the CSAT3B and IRGAs at the height of 2.87 m as measured from the soil surface to the central point of the sensors (Figure 2). We also considered $wind_{dir}$ for the tower setup because the physical structure of the tower has effects on surrounding airflows, including the distortion of the wind velocity and direction. Because of this, we oriented the CSAT3B to point at 184°S to maximize the exposure time for winds blowing from the prevailing wind directions, southwest (SW). These design guidelines are necessary to capture ≥ 80% contribution of the representative wetland, with the design goal of ≥ 90% contribution (Lee et al., 2004).

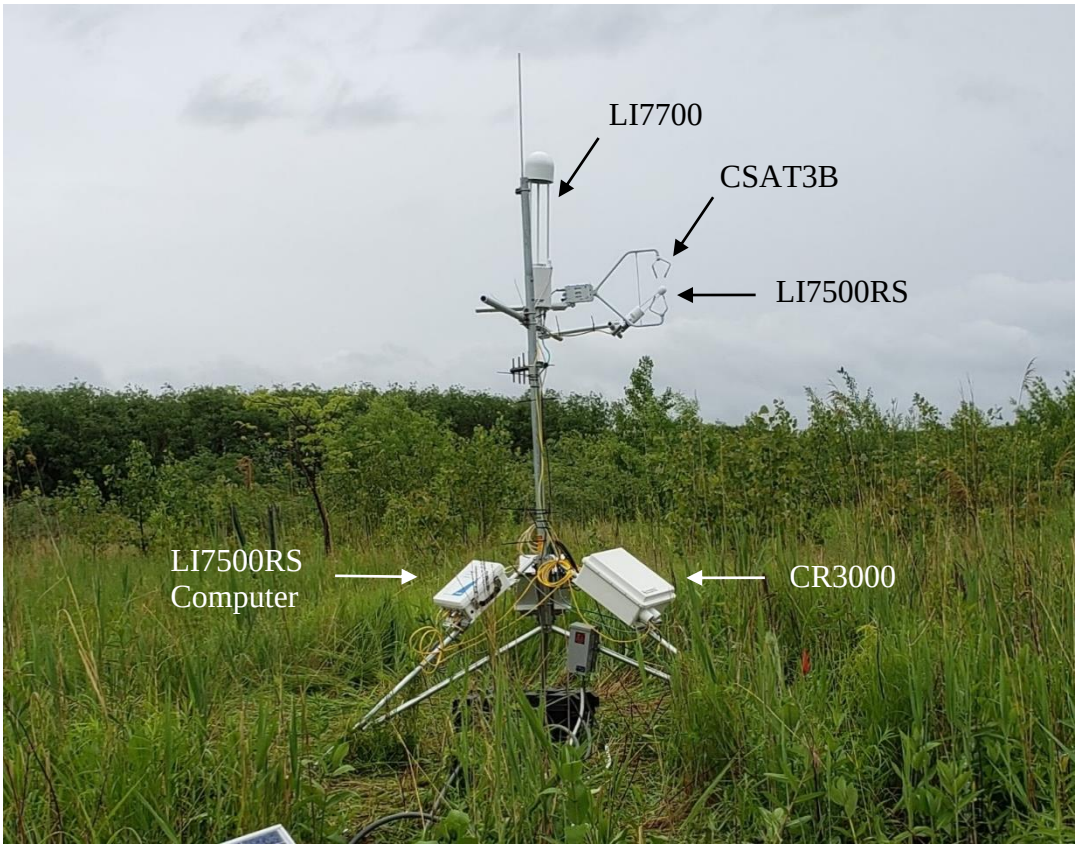

Figure 2. Open-path eddy-covariance tower configuration approximately 2.87 m above the inland salt marsh floor.

The LI-7500RS was placed 0.23 m upwind from the centralized point of the transducers on the CSAT3B with a slight angle from the vertical direction (~10-15°) to prevent water accumulation on the sensor's windows during rainstorms, as recommended by the LI-7500RS manual (LI-COR Biosciences, 2019). We installed the LI-7700 such that the center of the LI-7700 path was vertically aligned with the center of the CSAT3B transducers and was horizontally separated from the anemometer by 0.61 m. The sensor was oriented in a vertical mounting position to ensure 360° acceptance for $wind_{dir}$, as recommended by the LI-7700 manual (LI-COR Biosciences, 2020). The sensors were powered using photovoltaic cells installed 4.57 m from the tripod. The panels charged four 6V deep-cycle marine batteries with enough storage capacity for three days of power.

2.4 Flux Calculations

Flux measurements were calculated from the raw $wind_{speed}$ and gas concentration measurements using methods described originally in Morin et al., (2014b). In brief, we performed a 3-D coordinate rotation to the wind measurements to ensure the vertical and crosswind components average out to 0 for each 30-minute interval (Lee et al., 2004) and included the following corrections: (1) A lag correction accounting for the separation distance between the sonic anemometer and the IRGAs using the method of maximum covariance. (2) A spectral correction assessing for high-frequency data loss from IRGA path lengths (Massman, 2000). (3) Temperature correction for the dependence of the absorption spectrum of CO_2, CH_4, and water vapor (Kaimal and Gaynor, 1991), and (4) Webb, Pearman and Leuning (WPL) corrections to account for the changes in air density and water vapor for CO_2 and CH_4 concentrations (Webb et al., 1980). The corrections were completed on available despiked data.

Data were despiked using a series of filters. First, we filtered the data using internal diagnostic value information provided by the sensors to exclude situations when the measured concentration may not be reliable, as instructed by the manuals for LI-7700, LI-7500RS, and CSAT3B. We then evaluated data against seasonal maximum and minimum thresholds and identified and removed outliers by finding points six standard deviations away from the mean value of a measurement. A 30-minute interval is representative of the average surface exchange, capturing the major flux-carrying eddies (Farmer et al., 2006; Wolfe et al., 2009). The half-hour measurements were filtered using a friction velocity (u*) threshold of 0.1 ms^{-1}, to account for periods of insufficient turbulent mixing (Reichstein et al., 2005).

The hourly meteorological data were converted to half-hour measurements and gap-filled using a bi-linear, periodic, trended interpolation relationship (Morin et al., 2014b). This method considers the diurnal variation using the closest available values for each variable. The hourly cumulative rainfall measurements were not gap-filled in this fashion, but instead, the hourly measurement was applied to the final half-hour of each hour, and the initial half-hour was expressed as 0 mm. All meteorological data and flux measurements were categorized to day-night measurements based on the corresponding photosynthetically available radiation (PAR). PAR values greater than 10 W m^{-2} were determined to be day measurements. Otherwise, the value would be classified as night.

2.5 Footprint Model

We used a footprint model to estimate the land-source locations for the fluxes measured by the eddy-covariance tower. The footprint model is based on Morin et al., (2014b), an expansion of the 2-D model by Detto et al., (2006), which is built upon the 1-D model created by Hsieh et al., (2000). The model traces the probability that a parcel of air measured by the eddy-covariance tower derived from any point in the wetland using $wind_{speed}$, $wind_{dir}$, boundary-layer stability, and turbulence data. We overlaid the footprint model with the map of NDVI measurements to calculate a NDVI footprint-weighted total ($NDVI_{fwt}$), using a pixel resolution of one m^2 for each map for each 30-minute interval. The $NDVI_{fwt}$ is the integrated average NDVI value for each half-hour within the footprint contour bounds.

2.6 Modeling and Gap-filling of Fluxes

Following methods described in Morin et al., (2014a), artificial neural network (ANN) models were utilized to determine the empirical models for CH_4, GPP, and R_e as a function of climatological variables (e.g., meteorological data and $NDVI_{fwt}$) and to gap-fill the flux measurements. We used a forward-stepwise linear regression model, evaluated with the Akaike Information Criterion (AIC) - to determine the climatological variables that were included in the final ANN models. The variables were only included in the ANN model if they lowered the AIC score of the linear stepwise model. All meteorological data (T_{Air}, VPD, net_{Rad}, P_a, PPT_T, $wind_{speed}$, and $wind_{dir}$), u*, heat flux (LE), and the $NDVI_{fwt}$ were evaluated for each of the flux measurements. If a variable was selected by more than half of the forward-stepwise linear

regression models for a carbon flux, then we directly compared the variable against the carbon flux using pairwise linear regression.

The CO_2 (NEE) flux was partitioned into GPP and R_e. The nighttime NEE was used as the observed R_e values since no photosynthetic activity occurs then. We used an ANN to gap-fill the R_e for all missing values, including through the daytime (when no observations existed). The modeled R_e was subtracted from the NEE to calculate the GPP. The missing daytime GPP values were gap-filled using the ANN model. As defined in Rey-Sanchez et al., (2018), the ANN ran through 1000 iterations, and for each iteration, ANN chose an appropriate model if the model produced an $r^2 > 0.47$, $r^2 > 0.3$, and $r^2 > 0.7$ for R_e, CH_4, and GPP respectively. If the r^2 threshold was not met after 5000 attempts, ANN would accept a model with a r^2 greater than the mean of all r^2 +0.1. The final model was chosen based on an average of the top 10% iterations.

2.7 Lag Response

We also used the Granger causality test (G-causality) (Granger, 1969), to determine if the precipitation and atmospheric temperature time series were statistically significant predictors for the ecosystem's carbon exchange (CH_4, GPP, R_e). We used the G-causality package 2020 in MATLAB (version R2018a, MathWorks, Natick, MA). The package created two modeled time series of each flux: (1) Using an auto-regression function, and (2) Combining the autoregressive function with prior values for the variable tested for causation. We compared each model to the true fluxes, and then the BIC was calculated. When the multivariate model's (model 2) Bayesian Information Criteria (BIC) value significantly outperformed the univariate case (model 1), the driver was said to have a causal effect on the flux. The model's maximum time lag response for

the fluxes and drivers was set to 24 hours for the hour lag response to eliminate spurious correlation. If no lag response was determined on an hourly scale, the lag response of the carbon fluxes from T_{Air} and PPT_T events were assessed on a daily timescale with a maximum time lag response of 10 days. The causality of the drivers was evaluated based on hourly and daily intervals.

Chapter 3: Results and Discussion

3.1 Meteorological Conditions

Monthly rainfall ranged from 80 mm in July to 176 mm in October (Table 1), with the total precipitation during the observation period was 495.3 mm. The predominant $wind_{dir}$ was west south-west, with an average $wind_{speed}$ of 0.95 m/s (Figure 3). The stability of the $wind_{speed}$ and $wind_{dir}$ can be attributed to the wetland's location on top of SSB 14 (elevation 140 m) because the $wind_{speed}$ and $wind_{dir}$ is less likely to be distorted by ground surface shear stresses.

Table 1. Monthly and seasonal averages for the climatological variables (air temperature (T_{Air}), precipitation total (PPT_T), vapor pressure deficit (VPD), net radiation (net_{Rad}), friction velocity (u*), normalized difference vegetation idex footprint weighted total ($NDVI_{fwt}$), wind speed ($wind_{speed}$), wind direction ($wind_{dir}$), atmospheric pressure (P_a), and latent heat flux (LE)) used in the stepwise regression and neural network. The climatological variables were measured, averaged, and recorded on an hourly basis, while the eddy-covariance variables were measured, averaged, and recorded in 30-minute intervals. Therefore, the n values, listed in parentheses, for the climatological data is nearly half of the eddy covariance variables. PPT_T values are expressed as a summation for each timeframe. $Wind_{dir}$ values are expressed as the resultant vector average $Wind_{dir}$.

Variables		Jul.	Aug.	Sept.	Oct.	Nov.	Seasonal
		value (n)	value (n)	value (n)	value (n)	value (n)	value (n)
T_{Air}	°C	23.2 (744)	20.01 (744)	17.3 (720)	10.5 (741)	1.5 (312)	16.4 (3384)
PPT_T	mm	79.8 (744)	133 (744)	93.7 (720)	176 (741)	11.4 (312)	495 (3384)
VPD	hPa	818 (1358)	719 (1288)	703 (1125)	490 (1123)	367 (469)	669 (1260)
Net_{Rad}	W/m^2	138 (744)	113 (744)	85.1 (720)	27.6 (741)	4.64 (312)	85.7 (3387)
u*	m/s	0.170 (1443)	0.169 (1471)	0.186 (1361)	0.224 (1463)	0.273 (485)	0.194 (393)
$NDVI_{fwt}$	unitless	0.74 (1329)	0.74 (1279)	0.72 (1120)	0.75 (1133)	0.73 (442)	0.75 (1312)
$wind_{speed}$	m/s	0.802 (1443)	0.79 (1471)	0.84 (1361)	1.16 (1463)	1.52 (485)	0.95 (393)
$wind_{dir}$	deg	269 (1444)	268 (1471)	254 (1361)	241 (1463)	263 (485)	261 (392)
P_a	atm	0.99 (744)	0.99 (744)	0.99 (720)	0.99 (744)	0.99 (312)	0.99 (3384)
LE	W/m^2	92.97 (1338)	75.72 (1279)	60.65 (1116)	29.54 (1107)	17.60 (446)	63.58 (1331)

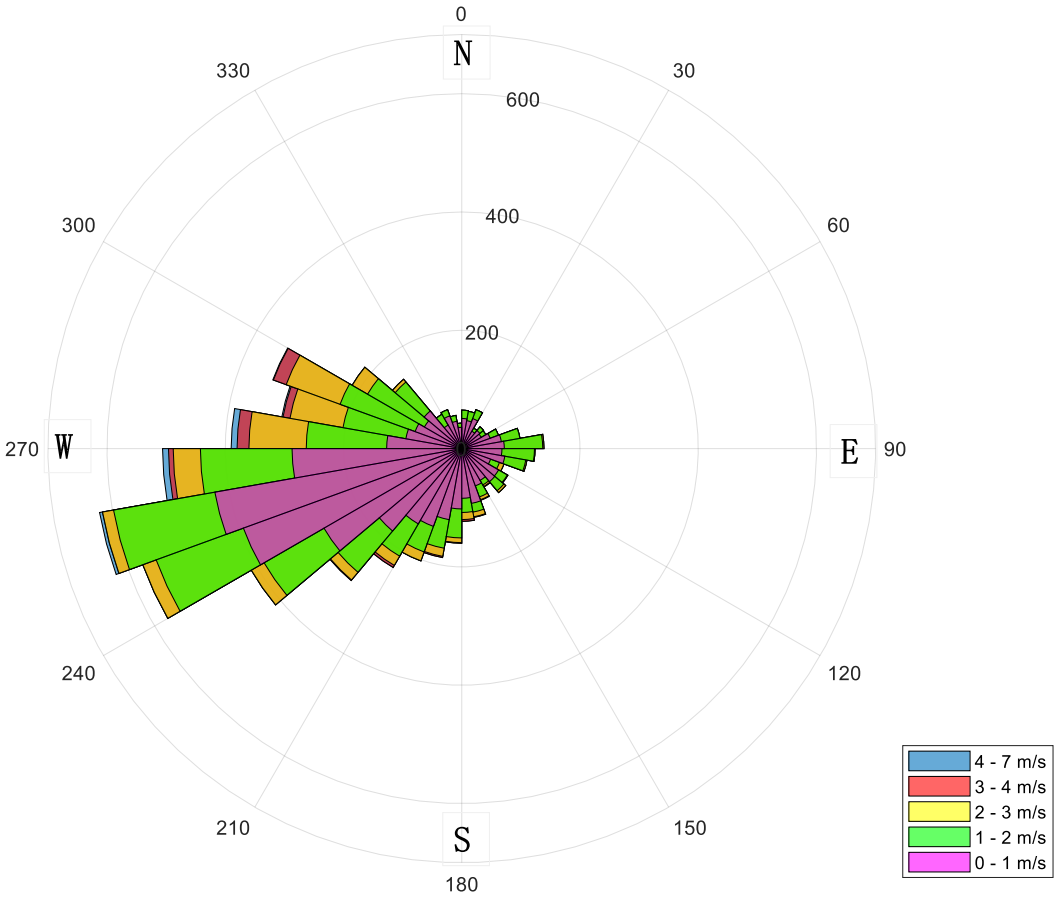

Figure 3. The direction (degrees) frequency and wind speed (m/s) of the 30-minute averaged observations from CSAT3B from June 27-November 11, 2019. The length of each "spoke" around the rings of the wind rose indicate the frequency (number of half-hour measurements) the wind blew in each direction and the color represents the speed. The primary wind direction ($wind_{dir}$) is west south-west and the average wind speed ($wind_{speed}$) is 0.95 m/s.

The time series represented in Figure 4a, Figure 5a, and Figure 6a, show the seasonal decrease in T_{Air}, net_{Rad}, and LE. The average T_{Air}, net_{Rad}, and LE ranged from 23°C – 1.5°C, 138 W/m^2 – 4.64 W/m^2, and 93 W/m^2 – 17.6 W/m^2, from July to November. The net_{Rad} observations were negative during the nighttime when there is no solar radiation and the net_{Rad} is dominated by the outgoing terrestrial longwave flux. The T_{Air} observations on October 1, 2019 (maximum of

29.5.6°C) were outside the whisker boundaries (90^{th} percentile) and were determined to be outliers for the month. The T_{Air} variation, represented as the box portion (25^{th} and 75^{th} percentile) of the boxplot was constant, Figure 4b, while the variation of the net_{Rad} and LE decreased through the season, Figure 5b and Figure 6b. The mean VPD and P_a were 669 hPa and 0.99 atm, respectively.

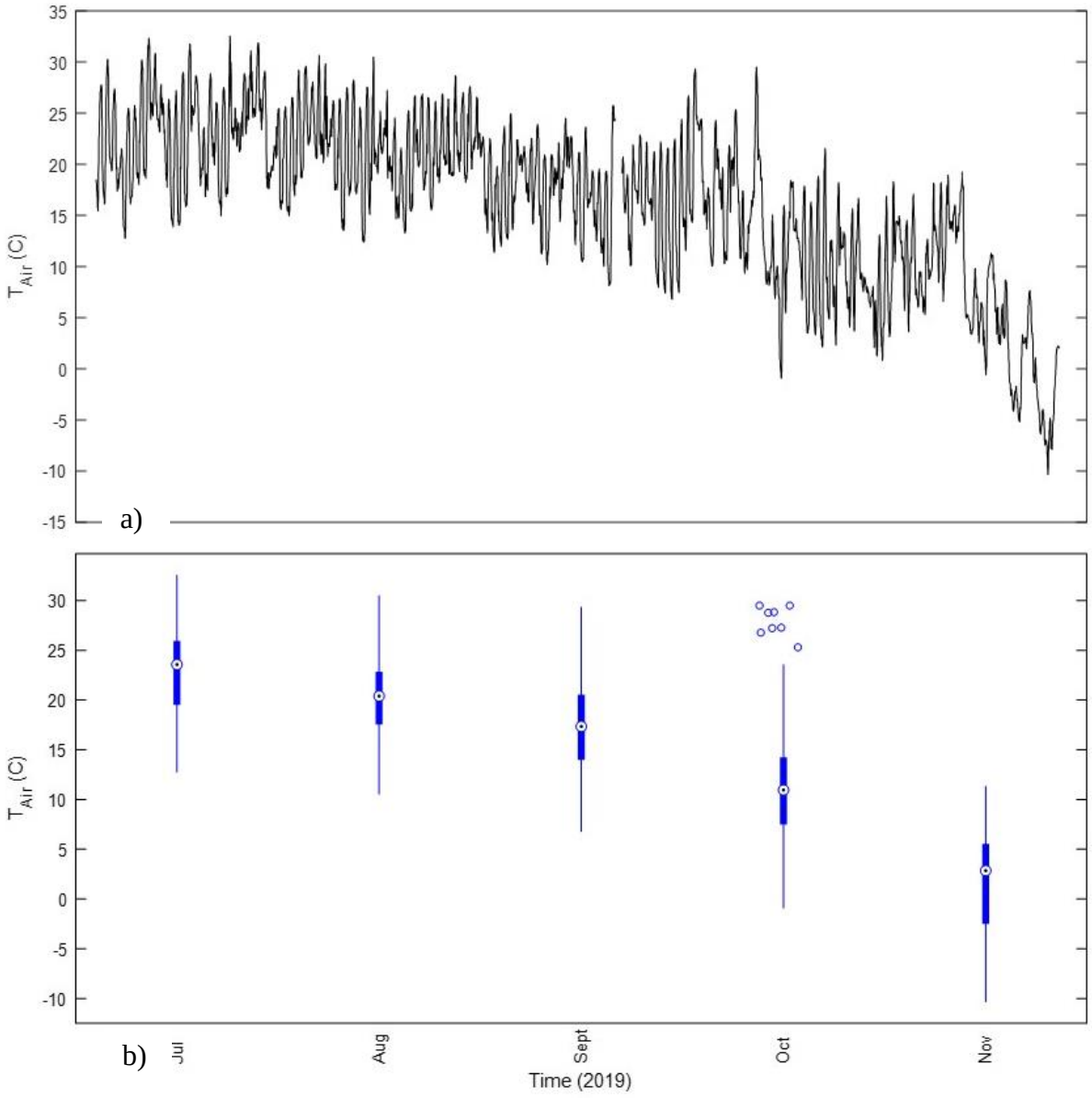

Figure 4. (a) Air temperature (T_{Air}) timeseries (one-hour intervals) from July 27 - November 11 2019. (b) Monthly T_{Air} variation expressed in a box and whisker plot. The bottom and top edges of the box plot indicate the 25^{th} to 75^{th} percentiles and the central mark (bullseye symbol) indicates the median. Each outlier (circle) represents an one-hour interval outside the 10^{th} and 90^{th} percentiles whisker boundaries.

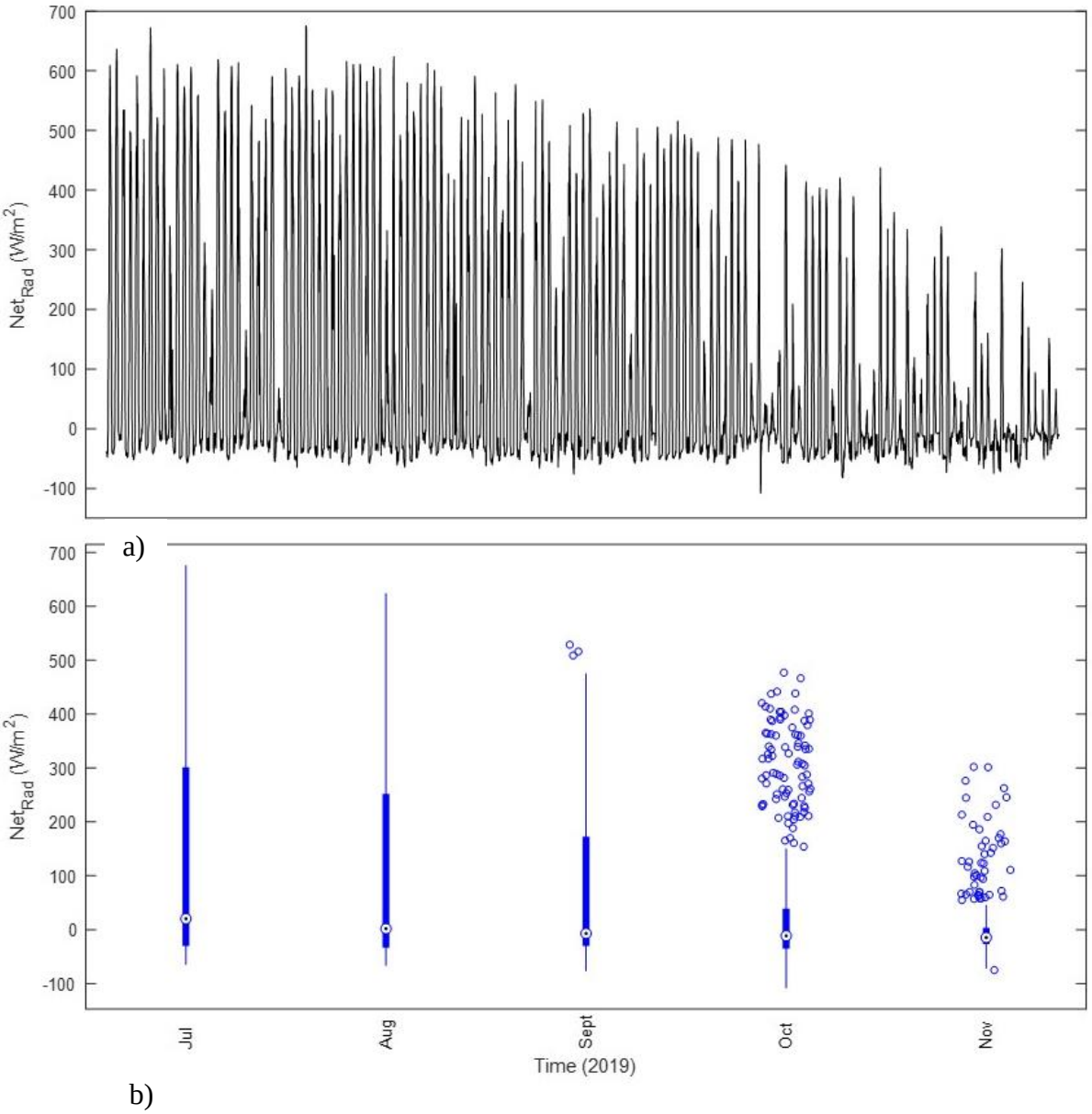

Figure 5. (a) Net radiation (net$_{Rad}$) timeseries (one-hour intervals) from July 27 - November 11 2019. (b) Monthly net$_{Rad}$ variation expressed in a box and whisker plot, The bottom and top edges of the box plot indicate the 25th to 75th percentiles and the central mark (bullseye symbol) indicates the median. Each outlier (circle) represents an one-hour interval outside the 10th and 90th percentiles whisker boundaries.

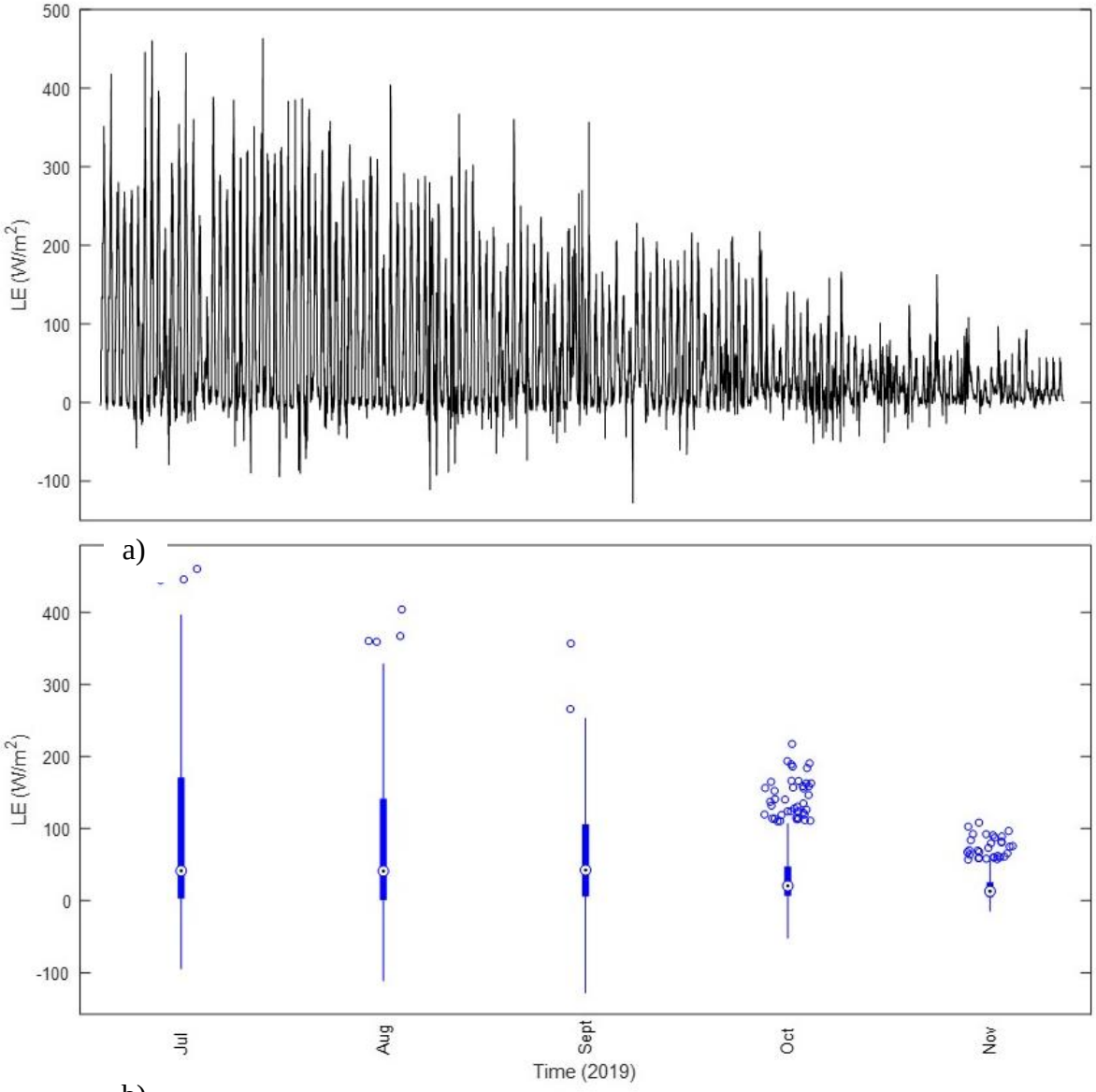

Figure 6. (a) Latent heat flux (LE) timeseries (30-minute intervals) from July 27 – November 11, 2019. (b) Monthly LE variation expressed in a box and whisker plot. The bottom and top edges of the box plot indicate the 25th to 75th percentiles and the central mark (bullseye symbol) indicates the median. Each outlier (circle) represents a 30-minute interval outside the 10th and 90th percentiles whisker boundaries.

3.2 Ecosystem Carbon Exchange

3.2.1 Methane

From June 27, 2019 to November 11, 2019, we measured CH_4 fluxes for 5,471 of a possible 6,768 half-hours. The neural network gap-filled the remaining 1,297 samples of the CH_4 flux (see Figure 7 for final modeled time-series). CH_4 fluxes ranged from -0.18 $\mu mol \cdot m^{-2} \cdot s^{-1}$ to 0.22 $\mu mol \cdot m^{-2} \cdot s^{-1}$ (both extrema occurring in September) with a mean flux of 0.002 $\mu mol \cdot m^{-2} \cdot s^{-1}$ for the observational period. The mean CH_4 fluxes gradually decreased throughout the observational study, except for August. August's mean flux was lower than expected for the decreasing trend but within the range of an acceptable mean flux. Since the mean flux does not account for winter months (which typically have low magnitude CH_4 emissions), we expect the annual mean flux to be lower than what was measured for the observational period. Seasonal emissions differ among ecosystem types (Ortiz-Llorente and Alvarez-Cobelas, 2012). The Solvay CH_4 fluxes are lower in magnitude than those reported for many freshwater systems but are comparable to observed in brackish and saltwater wetland systems (Table 2).

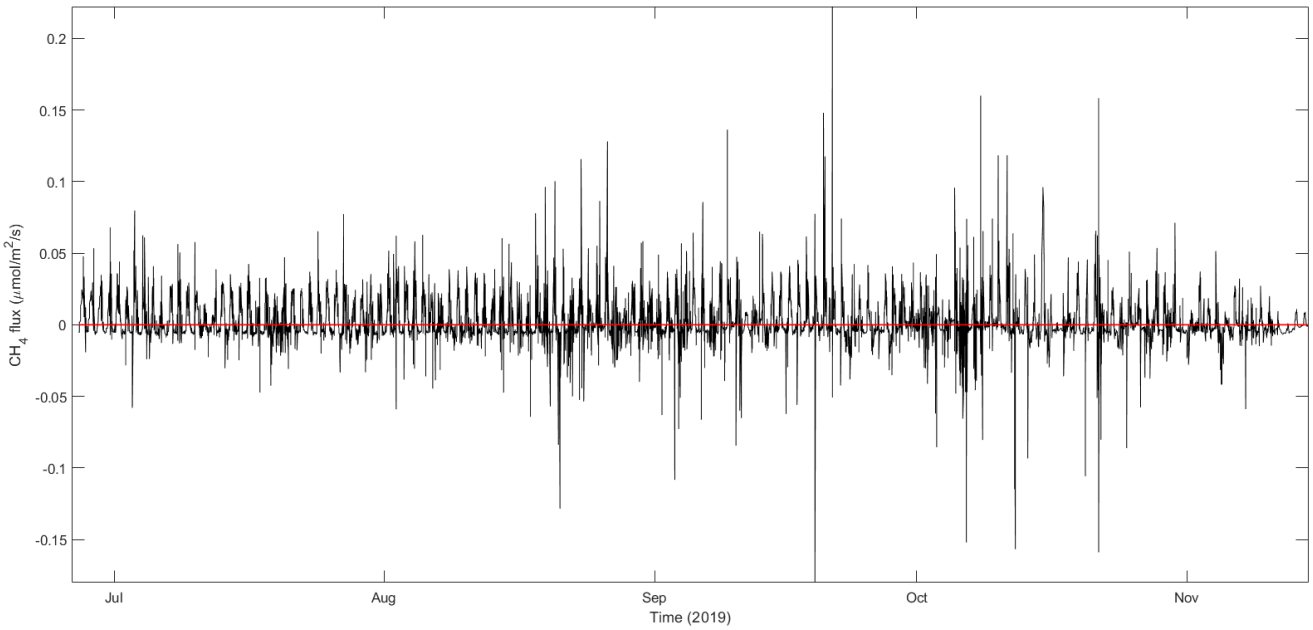

Figure 7. Overall modeled CH_4 fluxes from June 27 – November 11, 2019. The modeled CH_4 fluxes shows the best model for filling in the despiked CH_4 fluxes using the neural network.

Table 2. CH_4 fluxes from ranging ecosystems. CH_4 fluxes were captured using the eddy covariance (EC) technique or flux chambers (FC).

Wetland Type	Location	Timeframe	Technique	Mean CH_4 ($\mu mol \cdot m^{-2} \cdot s^{-1}$)	Citation
Solvay inland salt marsh	Camillus, NY	Jul. – Nov., 2019	EC	-0.18 – 0.222	This study
Freshwater marsh	Boutte, LA	Annual, 1992-1994	FC	0.035 – 0.65	Alford et al., 1997
Freshwater estuarine marsh	Lake Erie, OH	Jun. – Oct., 2016 & Apr. – Oct., 2016	EC	0.03 – 1.6	Rey-Sanchez et al., 2018
Tidal freshwater marsh	Waccamaw, SC	May 2008 to Jan. 2010	FC	0.28 – 0.83	Neubauer, 2013
Temperate Salt Marsh	Ribble, North-west England	Sept. 2010 – Aug. 2011	FC	0.00017- 0.022	Ford et al., 2012

3.2.1.1 Methane Regression Model

The forward stepwise regression model trained on 1,297 CH_4 flux samples. We used only half-hours where there were valid measurements for all potential empirical drivers and the CH_4 fluxes. The model determined different relationships between climatological variables and the carbon fluxes for each month and the season; however, some general season trends emerged (Table 3). For each timeframe, the selected variables were included in the final ANN model. Ultimately, the r^2 for the seasonal CH_4 flux model improved from 0.23 using the forward stepwise regression to 0.27 using the ANN model.

Table 3. Monthly and seasonal CH_4 fluxes and climatological variables (air temperature (T_{air}), total precipitation (PPT_T), vapor pressure deficit (VPD), net radiation (net_{Rad}), friction velocity (u*), normalized vegetation difference index ($NDVI_{fwt}$), wind speed ($wind_{speed}$), wind direction ($wind_{dir}$), atmospheric pressure (P_a), and latent heat flux (LE)). The statistical relationship between the CH_4 fluxes and the climatological variables were determined through stepwise regression and were included in the neural network to determine the represented final modeled fluxes for each timeframe. The model's stepwise regression order is the number listed in each of the columns.

	Jul	*Aug*	*Sept*	*Oct*	*Nov*	*Seasonal*
n	417	396	368	352	153	1734
$\mu mol \cdot m^{-2} \cdot s^{-1}$	0.0036	0.0021	0.0035	0.0006	0.0003	0.002
$gC \cdot m^{-2} d^{-1}$	0.004	0.002	0.004	0.001	0.000	0.002
$gC \cdot m^{-2}$	0.114	0.067	0.109	0.019	0.004	0.328
T_{air}	2		3	3		3
PPT_T					3	
VPD	3			4	2	
net_{Rad}	4		5	1	1	4
*u**					7	
$NDVI_{fwt}$			7			5
$wind_{speed}$			6	5	6	
$wind_{dir}$			4		4	
P_a		2	2		8	2
LE	1	1	1	2	5	1
Stepwise r^2	0.45	0.27	0.36	0.17	0.69	0.23
Neural Network r^2	0.48	0.27	0.37	0.21	0.54	0.27

T_{Air}, net_{Rad}, P_a, and LE were identified to have a significant explanatory effect for more than half of the monthly models while also being chosen for use in the final seasonal timeframe model. We further tested these particular variables directly against CH_4 using a pairwise regression to explore the underlying reasons behind the linkage (Figure 8). Other variables, including $wind_{dir}$, $wind_{speed}$, VPD, u*, and PPT_T were rejected from the final ANN model for the seasonal fluxes since their addition did not significantly improve the model. VPD and $wind_{speed}$ were selected to have a significant explanatory effect for three of the months, where PPT_T and u* were only chosen to affect November.

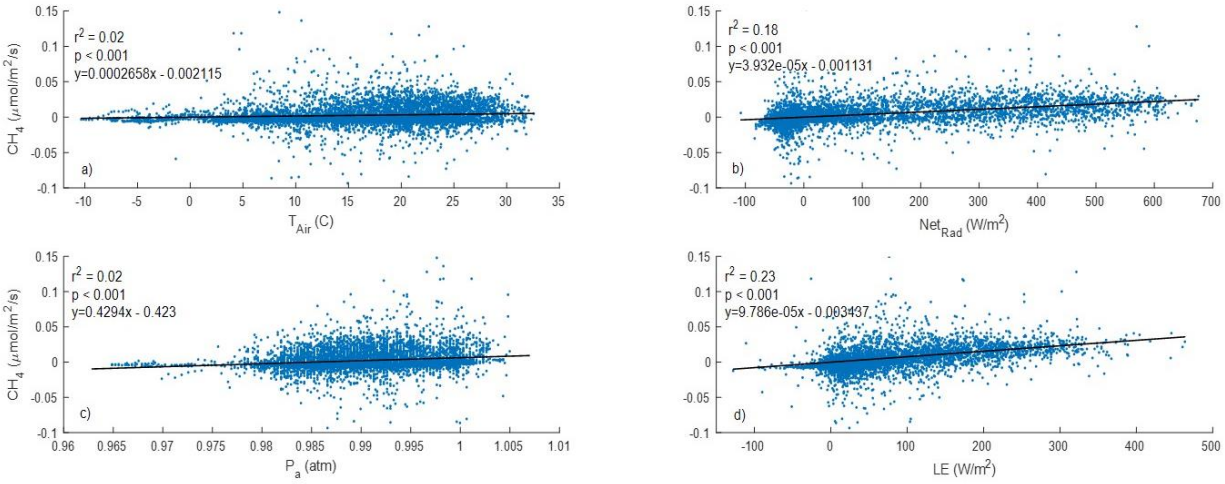

Figure 8. Pairwise relationships between the CH_4 fluxes and a) air temperature (T_{Air}), b) net radiation (net_{Rad}), c) atmospheric pressure (P_a), and d) latent heat flux (LE). The stepwise regression models (Table 3) selected T_{Air}, net_{Rad}, P_a, and LE to have a significant explanatory effect for more than half of the monthly and seasonal models.

LE and CH_4 fluxes were significantly correlated (r^2 = 0.23, $p<0.001$), and LE was the single most powerful statistical associate of CH_4 fluxes. LE was also the only variable to be selected for every monthly and seasonal stepwise regression model. This is comparable to the findings of Morin et al., (2014a), which demonstrated that LE was the strongest statistical associate for CH_4 fluxes during the daytime. Morin et al., (2014a) hypothesized that this relationship is a product of (1) an increase of the volatilization of methane and (2) the relationship between the stomatal conductance of water vapor and the methane transport through plant tissue. The pairwise regression (Figure 8d) indicates a positive relationship between LE and CH_4 fluxes, which is consistent with those findings. However, there was no standing water present at Solvay, which may indicate a stronger linkage with vegetative transmission since CH_4 transport from volatilization requires standing water.

Similar to LE, the pairwise relationship of net_{Rad} and CH_4 fluxes was positive (r^2 = 0.18, $p<0.001$) (Figure 8b). Incoming radiation and LE drive many of the same mechanisms. Increased net_{Rad} increases photosynthesis of the vegetation, resulting in the release of water vapor through the stomata pore, therefore, increasing LE (Ball et al., 1987). The stepwise regression identified net_{Rad} as a statistical associate for every month and for the season, except for August, which had anomalously low CH_4 fluxes that did not follow the seasonal trend (Table 3). The net_{Rad} in August was in par with the decreasing seasonal trend (Figure 8b). For October and November, net_{Rad} was the first variable added to the model. These were the only months that LE was not the first variable added to the stepwise regression models for CH_4, further showing the connection between LE and net_{Rad} at the site.

Our findings also found that T_{Air} had a significant explanatory effect on the CH_4 emissions, consistent with other studies (Bloom et al., 2010; Bohn et al., 2007; Chu et al., 2014; Rey-Sanchez et al., 2018). T_{Soil} is commonly cited as an environmental driver of CH_4 fluxes in wetlands due to its impact on microbial processes. Increased T_{Soil} promotes an increase in competing metabolic interactions between anaerobic methanogenesis (CH_4 production) and aerobic methanotrophy (CH_4 consumption). The model selected T_{Air} to have a significant explanatory effect for July, September, and October and the season. It was consistently the 3rd variable added to the stepwise models. The linear regression shown in Figure 8a resulted in a slightly positive pairwise relationship with CH_4 flux ($r^2 = 0.02$, $p < 0.001$) for the season.

Interestingly, P_a was added as the 2nd variable to the stepwise regression models for the season and for August and September, and the 8th variable added to the model for November. The pairwise linear regression between CH_4 fluxes and P_a (Figure 8c) showed a slight positive relationship ($r^2 = 0.02$, $p < 0.001$). There is one reported hypothesis that P_a has a significant effect on CH_4 emissions through CH_4 transport; falling pressure destabilizes bubbles and transports CH_4 by increasing CH_4 ebullition (Tokida et al., 2007). However, this relationship requires standing water and would have resulted in a negative correlation. Therefore, we hypothesize that the primary interaction effects between the ecological drivers may be the primary way that P_a interacts with CH_4 at our site.

3.2.2 Carbon Dioxide

The NEE of CO_2, as measured by the eddy-covariance tower, is the combination of two distinct processes: R_e and GPP. Here, we have 3,609 of a possible 6,768 valid half-hour measurements of

NEE. The remaining 3,159 values were gap-filled by the neural network (gap-filled time series shown in Figure 9). The NEE fluxes ranged during the season from -30.93 μmol·m^{-2}·s^{-1} (in July) to 28.95 μmol·m^{-2}·s^{-1} (in August) with a mean flux of 0.1954 μmol·m^{-2}·s^{-1} for the observational period (Table 4). This indicated that the CO_2 behavior of the site was a slight carbon source, which is comparable to the findings of Lu et al., (2017), who found that the average inland wetland was typically small CO_2 sinks or was nearly CO_2 neutral. This is consistent with the other reported NEE fluxes from freshwater wetlands sites (Table 5).

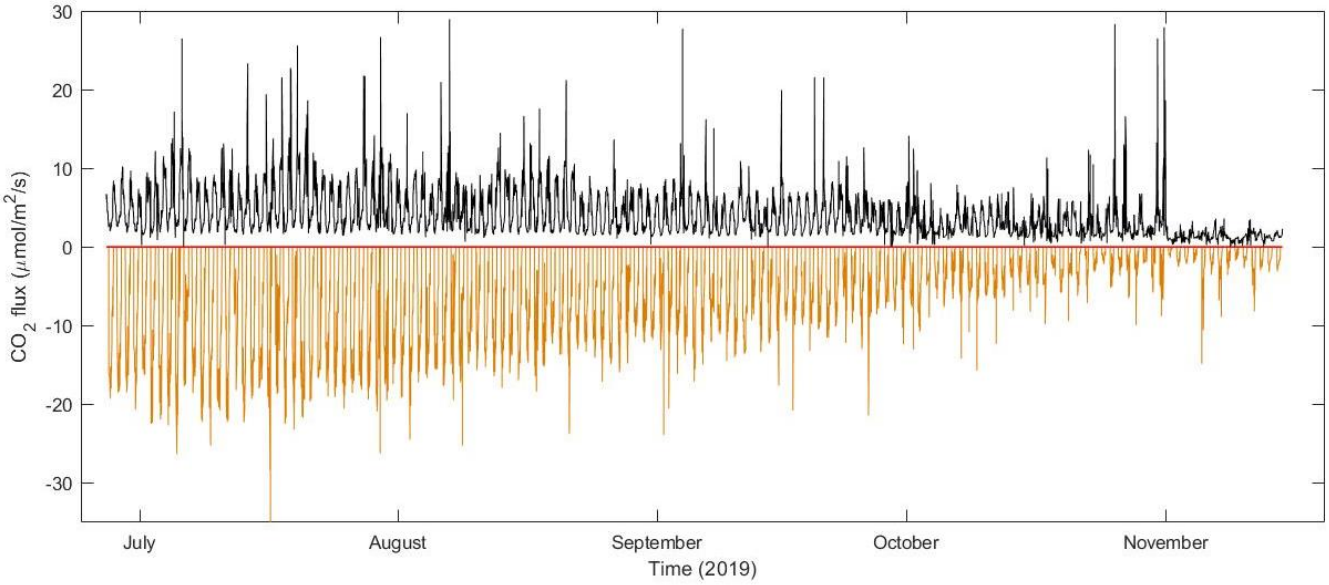

Figure 9. Final modeled NEE split into GPP (Orange) and R_e (Black) fluxes from June 27 – November 11, 2019. The red line indicates zero flux, for reference.

Table 4. Final modeled monthly and seasonal NEE (GPP + R_e) fluxes from the neural network. The n values are based on the rows included in the stepwise regression.

	Jul	*Aug*	*Sept*	*Oct*	*Nov*	*Seasonal*
n	406	381	373	361	163	1711
$\mu mol \cdot m^{-2} \cdot s^{-1}$	-1.25	0.68	0.71	1.83	0.22	0.20
$gC \cdot m^{-2} \cdot d^{-1}$	-1.3	0.7	0.7	1.9	0.2	0.2
$gC \cdot m^{2}$	-40.2	21.9	22.2	58.8	3.0	28.6

Table 5. NEE fluxes from ranging ecosystems. NEE fluxes were captured using the eddy covariance (EC) technique or close flux chambers (FC).

Wetland Type	Location	Date	Technique	NEE ($\mu mol \cdot m^{-2} \cdot s^{-1}$)	Citation
Solvay inland salt marsh	Camillus, NY	Jul. – Nov., 2019	EC	0.2	This study
Freshwater swamp marsh	Southern Finland	Jul. 2004 – Dec. 2005	EC	0.15	Aurela et al., 2007
Freshwater marsh	Everglades, FL	Apr. 2008 – Aug., 2009	FC	2.92	Schedlbauer et al., 2012
Alpine tundra wetland	Zoige, China	Jan. 2008 – Dec., 2000	EC	0.17	Hao et al., 2011
Tidal salt marsh	Hog Island, VA	Jul. – Aug., 2007	EC	-10	Kathilankal et al., 2008
Freshwater coastal marsh	Panjin, China	Jan. – Dec., 2005	EC	0.17	Zhou et al., 2009

The monthly NEE fluxes indicated the site was a sink (negative flux) for CO_2 in July and a source (positive flux) for CO_2 in the remaining months (Table 4). The variation in the diurnal pattern lessens over the time series, showing high variation during the beginning months and less variation during the end of the observational period (Figure 10). The high diurnal variability during the summer months is due to elevated daytime photosynthesis (i.e. high GPP) and

elevated microbial and autotrophic respiratory processes (i.e. high R_e). The mean R_e (4.07 $\mu mol \cdot m^{-2} \cdot s^{-1}$) from the inland salt marsh was higher than the mean GPP uptake (-3.87 $\mu mol \cdot m^{-2} \cdot s^{-1}$), resulting in the site being a slight CO_2 source of 28.6 $gC \cdot m^2$ of CO_2 throughout the study. The GPP and R_e were consistent with other observational studies (Chu et al., 2014; Hinojo-Hinojo et al., 2016) that reported their GPP and R_e fluxes during the growing season to be 326.7 – 933 $gC \cdot m^{-2}$ and 282.8 – 561 $gC \cdot m^{-2}$, respectively. It is worth noting that the CO_2 source behavior of the site is only reflective of the observational period and does not describe the behavior of the site on an annual timescale. We anticipate that the wetland would take in CO_2 during the early growing season but would emit CO_2 during the winter (Wang et al., 2013). Because of this, the true annual CO_2 flux behavior cannot be determined here, but our results suggest that the site is likely a slight source of CO_2 to the atmosphere.

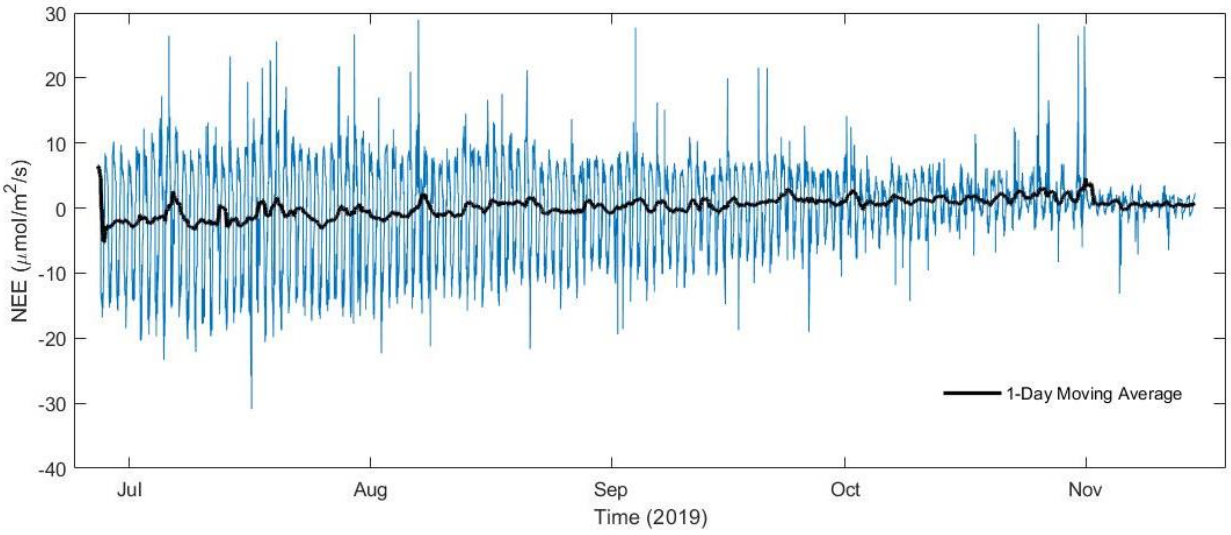

Figure 10. Final modeled NEE fluxes from June 27 – November 11, 2019. The 1-day moving average shows the shift in the carbon behavior from a carbon sink in July to a slight carbon source in September.

3.2.2.1 Gross Primary Production Regression Model

We used 1,114 GPP flux samples in the forward-stepwise regression model to determine the relationship between the climatological variables and GPP (Table 7). Like CH_4, we used only half-hours where there were valid measurements for all climatological variables and GPP fluxes. The GPP models showed to have the most statistical associates per timeframe out of the carbon fluxes (CH_4, GPP, and R_e), especially for the seasonal timescale where the stepwise regression model selected all but PPT_T to have a significant explanatory effect on GPP. Over half the monthly and seasonal models selected T_{Air}, P_a, LE, VPD, net_{Rad}, and $wind_{dir}$ as statistical associates for GPP (Table 6). We used a pairwise regression to test each of these variables against GPP for insight into the underlying cause of the correlation (Figure 11). The pairwise regressions showed the strongest trend between GPP and LE (Figure 11c: $r^2 = 0.66$, $p < 0.001$), followed by GPP uptake and T_{Air} (Figure 11b: $r^2 = 0.26$, $p < 0.001$), net_{Rad} (Figure 11b: $r^2 = 0.26$, $p < 0.001$), and VPD (Figure 11d: $r^2 = 0.25$, $p < 0.001$), all of which showed a positive relationship. Also, LE, net_{Rad}, and VPD were consistently the 1st, 2nd, and 3rd variables added to the models; the order in which T_{Air} was added varied month to month. The strong trends and positive relationships between GPP uptake and LE, VPD, and net_{Rad} are consistent with findings of other observational studies which reported that CO_2 uptake was tightly correlated with LE and net_{Rad} and the relationship between the climatological variables themselves (Baker et al., 2003; Schäfer et al., 2014). LE itself may not be an actual driver of GPP, but may share the same underlying drivers with GPP, resulting in a strong agreement.

Table 6. Monthly and seasonal GPP fluxes and climatological variables (air temperature (T_{air}), total precipitation (PPT_T), vapor pressure deficit (VPD), net radiation (net_{Rad}), friction velocity (u*), normalized vegetation difference index ($NDVI_{fwt}$), wind speed ($wind_{speed}$), wind direction ($wind_{dir}$), atmospheric pressure (P_a), and latent heat flux (LE)). The statistical relationship between the GPP fluxes and the climatological variables were determined through stepwise regression and were included in the neural network to determine the represented final modeled fluxes for each timeframe. The stepwise regression order is expressed by the number listed in each of the columns.

	Jul	*Aug*	*Sept*	*Oct*	*Nov*	*Seasonal*
n	294	277	252	199	75	1114
$\mu mol \cdot m^{-2} \cdot s^{-1}$	-7.66	-5.81	-3.72	-1.95	-1.13	-3.87
$gC \cdot m^{-2} \cdot d^{-1}$	-7.94	-6.02	-3.85	-2.03	-1.17	-4.02
$gC \cdot m^{2}$	-246	-187	-116	-62.8	-15.17	-566
T_{air}	2		6	4		6
PPT_{Total}		7	7		1	
VPD		5	3	3	5	3
net_{Rad}	5	2	4	2	2	2
*u**					3	8
$NDVI_{fwt}$		4			6	5
$wind_{speed}$			5		4	9
$wind_{dir}$	3	3			7	4
Pa	4	6	2			7
LE	1	1	1	1	8	1
Stepwise r^2	0.81	0.84	0.51	0.71	0.84	0.86
Neural Network r^2	0.81	0.70	0.65	0.67	0.77	0.82

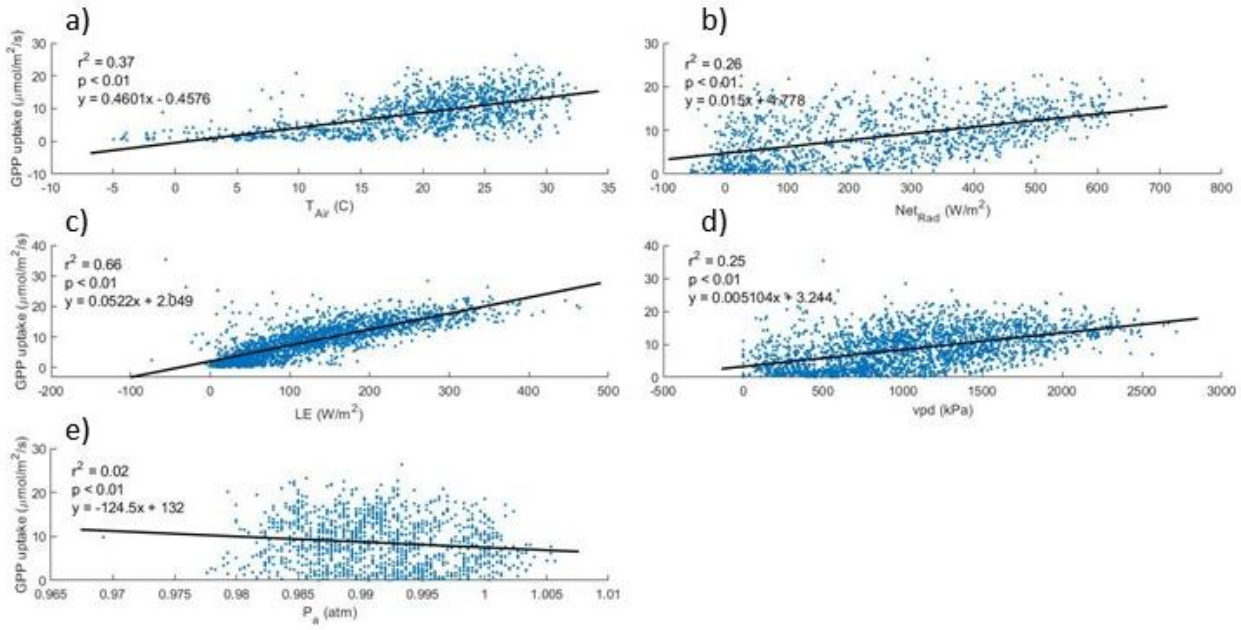

Figure 11. Pairwise relationships between the GPP fluxes and a) air temperature (T_{Air}), b) net radiation (net_{Rad}), c) latent heat flux (LE), d) vapor pressure deficit (VPD), and e) atmospheric pressure (P_a). The stepwise regression models (Table 6) selected T_{Air}, net_{Rad}, LE, VPD, and P_a to have a significant explanatory effect for more than half of the monthly and seasonal models.

Net_{Rad} is the primary driver of photosynthesis (Frolking et al., 1998; Lafleur et al., 2001; Lund et al., 2009). During periods of high net_{Rad}, there is high light availability which promotes photosynthesis in well-watered plants, causing low CO_2 concentrations within the plant, and therefore, maximizing the stomatal conductance rate. Stomatal conductance is the rate at which CO_2 enters (GPP) uptake, and water vapor (LE) exits through the stomate pores on the leaves. This is confirmed in our findings, where Figure 11b shows a positive relationship with daytime GPP uptake.

Stomata conductance regulates GPP and LE (Ball et al., 1987) through transpiration by the plant leaves and explains (1) the strong positive relationship that we found between GPP uptake and LE in the pairwise regression (Figure 11c) and (2) the selection of LE as the 1st variable to be added to the stepwise regression models (Table 6). GPP is mechanistically linked to LE, via

transpiration, since a plant that absorbs lots of carbon through photosynthesis will also transpire a lot. Because of this, we would expect that both variables would be driven by the same climatological variables (e.g., VPD and net_{Rad}) and would naturally be correlated, although neither was directly responsible for the other. Our stepwise model behaved as would be expected for this behavior, selecting VPD as the third variable, following LE and net_{Rad}, and showed a positive effect on GPP uptake in Figure 11d. VPD drives the stomata conductance (Penman, 1948) by providing the impetus for water diffusion across the stomate pore. However, many plants will reduce stomatal conductance during periods of high VPD between the leaf and the atmosphere to minimize water loss and to retain the hydration of the plant cells. The exact effect that VPD imposes on LE is dependent on the state as well as the change in VPD. If the initial VPD is low and increases, then the LE will also increase since the positive effect of VPD outweighs the negative effect. If the VPD is initially high and increases further, though, then the LE will decrease since the negative effect will outweigh the positive effect. These findings show that the relationships between net_{Rad}, VPD, and LE are not static, but instead, the impact of one variable depends on the variations of the other climatological variables.

T_{Air} also had a positive correlation with daytime GPP uptake ($r^2 = 0.37$, $p < 0.001$), Figure 11a, which is expected since T_{Air} increases during the springtime and through the growing season, similar to net_{Rad}, so the two variables would be correlated absent direct driving behavior. However, vegetation vigor is also linked to T_{Air} (Xiao and Moody, 2005), indicating possible causation and not merely a correlation. The peak magnitude of GPP occurred on July 16th (-35.31 $\mu mol \cdot m^{-2} \cdot s^{-1}$), which is also the date with the highest recorded hourly temp (32.°C) during the observational period. The mean T_{Air} on July 16, 2019 was 4.1°C cooler than the daily high T_{Air}

of 27.5°C that occurred on July 20, 2019. Surprisingly, the highest daily mean GPP (-8.22 $\mu mol \cdot m^{-2} \cdot s^{-1}$) occurred on July 20th, supporting T_{Air}'s negative relationship with GPP. Hofstra and Hesketh et al., (1969) reported that cool-climate species had the widest apertures around 27 to 30°C. Stomata are not expected to close down unless T_{Air} reaches 36°C under water-stressed conditions, which was never the case during the observational study. During colder T_{Air} periods with lower net_{Rad}, the vegetation growth and GPP uptake potential decrease.

The stepwise regression also identified P_a and $wind_{dir}$ to be other statistical associates for GPP. Shifts in P_a are not reported in the literature to impact GPP, but it is related to VPD and T_{Air}. P_a is determined by the weight of the air above where the measurement was taken (Priestley, 1946), and the weight of the air varies with inversely with T_{Air}. Typically, warm air rises and causes a decrease in surface pressure. Localized precipitation events or increased evaporation can also cause changes in P_a. P_a decreases with precipitation but increases with evaporation. Therefore, the stepwise regression may be using P_a as a proxy variable for a collection of other variables rather than suggesting that it is itself a direct driver of GPP.

3.2.2.2 Ecosystem Respiration Regression Model

For R_e, the model identified T_{Air}, LE, and $NDVI_{fwt}$ to have a significant explanatory effect for more than half of the monthly and seasonal timeframes (Table 7). We tested each of these variables against R_e using pairwise regressions to determine the significance of the trends (Figure 12). The stepwise model consistently added T_{Air} into the model as the first variable for all timeframes and T_{Air} was the only variable tested in pairwise regression to show a trend (Figure

12a). The positive relationship between T_{Air} and R_e, indicated that increased T_{Air} resulted in increased R_e at the site, consistent with the findings of Niu et al., (2012); Raich and Schlesinger et al., (1992); Schäfer et al., (2014); Singh and Gupta et al., (1977). Even though the positive trend between R_e and T_{Air} is well documented, there is no agreement on the exact form of the relationship (e.g., people hypothesize the linkage may be a linear relationship (Froment, 1972; Witkamp, 1966), Q10 exponential relationship (Hoff, 1898), or an exponential dependence (Raich and Schlesinger, 1992)). Lloyd and Taylor et al., (1994) compared the methods and found that an Arrhenius type equation where the effective activation energy for R_e varies inversely with T_{Air} accurately represents the relationship between R_e and T_{Air}.

Table 7. Monthly and seasonal R_e fluxes and climatological variables (air temperature (T_{air}), total precipitation (PPT_T), vapor pressure deficit (VPD), net radiation (net_{Rad}), friction velocity (u*), normalized vegetation difference index ($NDVI_{fwt}$), wind speed ($wind_{speed}$), wind direction ($wind_{dir}$), atmospheric pressure (P_a), and latent heat flux (LE)). The statistical relationship between the R_e fluxes and the climatological variables were determined through stepwise regression and were included in the neural network to determine the represented final modeled fluxes for each timeframe. The stepwise regression order is expressed by the number listed in each of the columns.

	Jul	*Aug*	*Sept*	*Oct*	*Nov*	*Seasonal*
n	112	104	121	162	88	597
$\mu mol \cdot m^{-2} \cdot s^{-1}$	6.41	6.49	4.43	3.78	1.35	4.07
$gC \cdot m^{-2} d^{-1}$	6.64	6.73	4.59	3.92	1.40	4.22
$gC \cdot m^2$	206	209	138	122	18.17	595
T_{air}	1	2	1	2	1	1
PPT_{Total}						
VPD				3	6	5
net_{Rad}					5	
*u**	3					4
$NDVI_{fwt}$	4		3	4	4	
$wind_{speed}$	2	1				2
$wind_{direction}$				5	2	
P_{Avg}						3
LE	5		2	1	3	
Stepwise r^2	0.30	0.20	0.18	0.37	0.58	0.47
Neural Network r^2	0.57	0.39	0.24	0.66	0.73	0.43

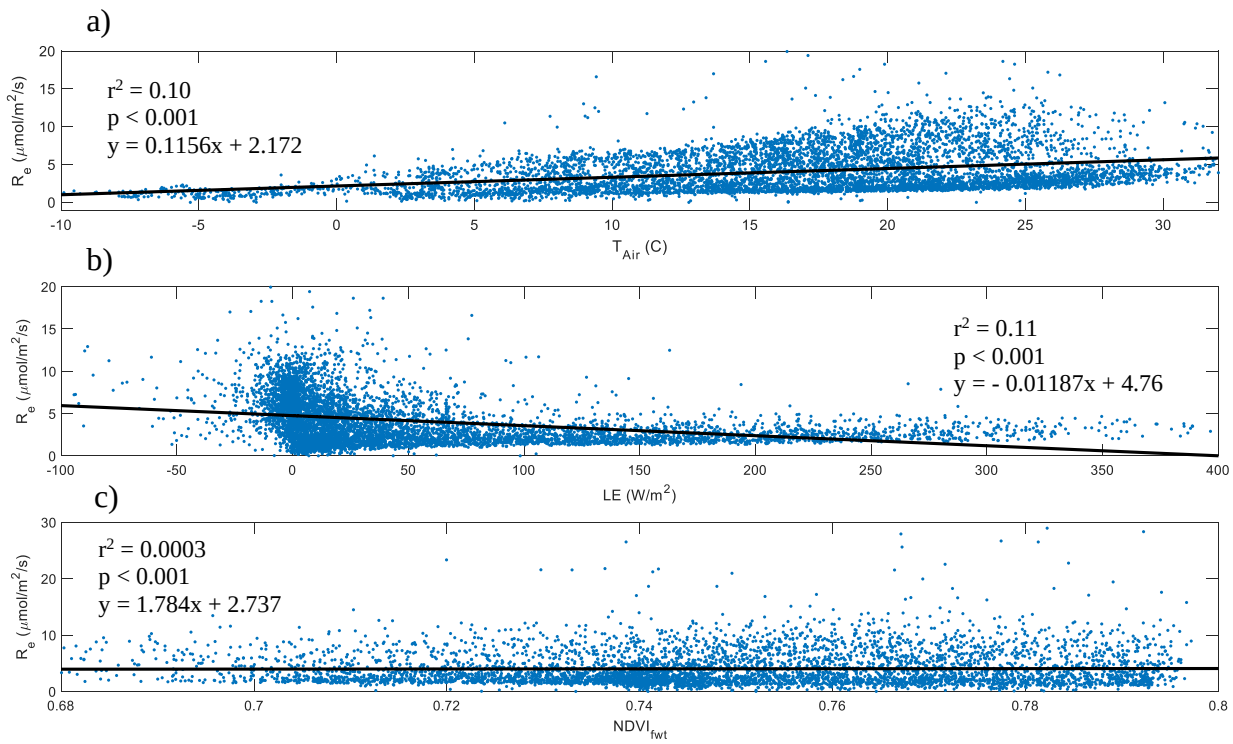

Figure 12. Pairwise relationships between the R_e fluxes and a) air temperature (T_{Air}), b) latent heat flux (LE), and c) normalized difference vegetation index footprint weighted total ($NDVI_{fwt}$). The stepwise regression models (Table 7) selected T_{Air}, LE, and $NDVI_{fwt}$ to have a significant explanatory effect for more than half of the monthly and seasonal models.

The uncertainty between R_e and T_{Air} is due to the complexity of R_e. R_e is made up of a variety of autotrophic (R_a) and heterotrophic (R_h) processes, and each component reacts differently to the changes in the ecological conditions (Bahn et al., 2010; Davidson and Janssens, 2006; Hopkins et al., 2013; Teskey et al., 2007; Trumbore, 2006). R_a is dependent on the carbon input from the canopy, while R_h is moderated by the carbon storage and nutrient content within the soil (Binkley et al., 2006). R_a contributes to a greater portion of ecosystem respiration in high-productivity sites than in low-productivity sites (Bond-Lamberty et al., 2004).

The NDVI has been proven to be a valuable tool to determine the productivity of sites as a proxy for leaf area index (Tucker, 1979), absorbed photosynthetically active radiation (Kumar and

Monteith, 1981), vegetation biomass (Sellers, 1987), R_e (Boelman et al., 2003), and NEE (Goward et al., 1985). The stepwise regression added the $NDVI_{fwt}$ into the model as the fourth variable and showed a slightly positive trend with Re through pairwise regression (Figure 12c: $r^2 = 0.003$, $p < 0.001$). Boelman et al., 2003 suggested that the positive correlation between NDVI and R_e could be attributed to the following relationships: (1) NDVI is a proxy for photosynthesis and a portion of photosynthesis produced goes to plant maintenance and growth respiration (Waring et al., 1998). (2) During peak season, the total plant biomass accounts for the majority of R_e (Johnson et al., 2000), and (3) High plant biomass has high litter production and, therefore, more labile carbon substrates for soil microbes. Further NDVI readings and an updated vegetation survey is required to dive into the relationship between $NDVI_{fwt}$ and R_e at the site.

The pairwise regression between LE and R_e showed no discernable trend (Figure 12b: $r^2 = 0.11$, $p < 0.001$). The order in which LE was added to the stepwise regression models for R_e varied month to month (Table 7), ranging from the first variable to be added to the model in October and the fifth variable to be added in July. This may indicate that the stepwise regression was picking up an interaction effect with other climatological variables that are dependent on LE and influence R_e, e.g., soil moisture or air and soil temperature.

3.3 Lag Response

We used the Granger Causality test to determine if T_{air} and/or PPT_T were a causal driver of the carbon fluxes (Table 8). The test was essential to avoid an assumption of causation to variables that simply exhibited a strong correlation, which could indicate a linkage via a shared third driver or could indicate pseudo replication due to the natural diurnal cycle of environmental variables.

The hourly lag response models were based on 3360 values, while the daily lag response models (only used in the event that no hourly lag response was detected) were based on 131 values. Similar to Sturtevant et al., (2016), we allowed a maximum lag of 24 hours when testing for hourly lag response, and 10 days when evaluating on a multiday scale. We determined that GPP, R_e, and CH_4 fluxes were all driven by T_{air}, showing a maximal covariance between three (R_e) to five (CH_4) hours after T_{air}. The Granger Causality test identified that GPP and R_e showed a hourly lag response from PPT_T. CH_4 fluxes exhibited a lag response to PPT_T on a daily scale (peak at one day) but not an hourly scale.

Table 8. Lag Responses of CH_4, GPP, and R_e caused by total precipitation (PPT_T) and T_{air} in units of hours or days based on the timeframe.

Caused	**Causal**	**N**	**Timeframe**	**Lag Response**	**P-value**	**Granger-Caused?**
CH_4	T_{air}	3360	Hourly	5	< 0.001	Yes
	PPT_T	3360	Hourly	1	0.0840	No
		131	Daily	1	< 0.001	Yes
GPP	T_{air}	3360	Hourly	4	< 0.001	Yes
	PPT_T	3360	Hourly	1	0.0215	Yes
R_e	T_{air}	3360	Hourly	3	< 0.001	Yes
	PPT_T	3360	Hourly	2	< 0.001	Yes

3.3.1 CH_4 lag responses

For CH_4, there was a lag response of five hours from T_{air}, which may be indicative of the time it takes for T_{air} to influence the soil temperature (T_{soil}). T_{soil} is widely supported as a driver of belowground ecosystem processes due to its effects on microbial respiratory processes. Lee et

al., (1978) found a four- to six-hour lag time between T_{soil} and T_{air} at a soil depth of 10 cm and also found that the exact lag time is influenced by topography, soil texture, and soil water content. The five-hour lag response between CH_4 and T_{air} found here agrees with that range, strongly suggesting the link is ultimately via the lag response of T_{air} on T_{soil}. This is also consistent with Reid et al., (2013) results that showed a lag between air and surface soil temperatures and depth-integrated CH_4 pools. Overall, our findings support our stepwise regression model, which identified T_{air} as one of the four climatological variables that showed a significant explanatory effect on the CH_4 fluxes, and indicated that CH_4 emissions increase with temperature (Figure 8).

The lag response of one day from daily PPT_T events could reflect changes in the water table depth and dissolved oxygen (DO) concentrations caused by PPT_T events. Water table fluctuations are dependent on the inputs (precipitation, surface flow, and groundwater inputs) and outputs (evapotranspiration, surface flow, and groundwater efflux) of the water budget, and are sensitive to environmental and climatic changes (Sollid and Sørbel, 1998). At the Solvay site the soil gravimetric water content approaches 70% of the volumetric soil content at saturation. In some portions of the wetland, there is an impermeable layer of compacted Solvay soil approximately 460 mm below the soil surface (D. Daley, personal communication, March 23, 2020). Therefore, during and after significant precipitation events, we assume PPT_T can be used as a proxy variable for water table depth since we expect nearly instantaneous shifts in the water table depth in response to PPT_T events. Chamberlain et al., (2017) reported that during PPT_T events, the DO concentrations increased to approximately 30 times the background concentrations within the water table and it took one day for the DO concentrations to reduce to

anoxic conditions (<1.0 $mg \cdot L^{-1}$) after the rainfall event. These findings are consistent with our lag response, indicating the site may take one day for the DO to deplete after PPT_T events and to favor methanogenesis.

3.3.2 CO_2 lag responses

We tested CO_2 fluxes for lag responses by first partitioning NEE into GPP and R_e since each component could hypothetically respond to environmental stimuli in distinct ways. Both exhibited a lag response to temperature with a maximal covariance lag time of four hours (GPP) and three hours (R_e) (Table 8), both with a positive pairwise slope (Figure 11 and Figure 12). R_e had the strongest relationship with T_{air} out of all the fluxes, as identified by the stepwise regression (Table 7). Like CH_4, the R_e emissions of the site are likely directly driven by T_{soil}, which is slowly influenced by T_{air}. Our lag response for GPP from T_{air} is consistent with Admirall et al., (1976) and Colijn and Van Buurt et al., (1975) who all found that hourly T_{air} had a significant effect on primary production and growth rates (though the impact of these short-term changes is species dependent (Admiraal, 1977)).

Both carbon fluxes also had a response to PPT_T. R_e and GPP had much faster responses to PPT_T events than CH_4 fluxes, with two- and one-hour responses, respectively. The fast lag response of GPP to PPT_T events is indicative of the water limitation at the site during the growing season. During drought conditions, PPT_T events decrease water stress on vegetation and promote photosynthesis, increasing CO_2 uptake by plants. GPP was the only CO_2 flux that the stepwise regression identified PPT_T to be an ecological driver for any of the months during the observational period, which could be suggestive of the low lag response of one hour. For GPP,

the stepwise regression identified PPT_T to be a statistical associate in August (7^{th} variable added), September (7^{th} variable added), and November (1^{st} variable added). Since PPT_T was not selected as a driver for GPP on a seasonal timescale, we cannot determine the relationship using pairwise regression for the observational period. PPT_T is a semi-discrete variable in that its value is zero except for during precipitation events. All other variables tested in this study were continuous, which may have discouraged the selection of PPT_T in favor of other variables.

R_e showed a two-hour lag response from PPT_T, which could be attributed to an increase in DO concentrations and soil moisture content during PPT events. Rainfall can increase the DO concentrations of the groundwater to approximately 30 times the background concentrations (Chamberlain et al., 2017) and, therefore, increase R_e with DO consumption. Many studies, Aerts and de Caluwe et al., (1997); Jeong et al., (2018); Meentemeyer et al., (1984), reported that R_e mainly depends on T_{soil} and soil moisture content. R_e emissions could hypothetically increase in response to both rising and falling water tables. During soil drying events, the cracking of organic colloids can increase the "water-soluble organic substrate" availability (Birch, 1959). During periods of high soil saturation, some soil microbes may experience cell lysis (i.e., breaking down of the cell wall) due to high turgor pressure resulting in the release of an organic substrate which surviving microbes will readily uptake (Kieft, 1987). Jeong et al., (2018) saw R_e increase immediately after hourly PPT_T events of 4.6 mm or more for up to two hours after the precipitation ended, and then R_e returned to normal levels.

3.4 Footprint Model and NDVI footprint weighted total

We determined the tower's cumulative footprint for day and night for each of the months and for the entire observational period (Figure 13). The footprints for each of the timeframes had little variability and were stable in direction due to consistent $wind_{dir}$ during the observational period (Table 1). The size of the footprint depended on the time of day (daytime versus nighttime) and month. The footprint increased in size throughout the observational period and at night; the smallest occurring during the daytime in July (Figure 13a) and the largest during the nighttime in October (Figure 13d). We attribute the larger footprint during the night time and during the shoulder season to weak turbulent mixing and a stable boundary layer from lower surface temperatures. These atmospheric characteristics also caused some variability in the smoothness of the ovular shaped contour lines (best seen in Figure 13d).

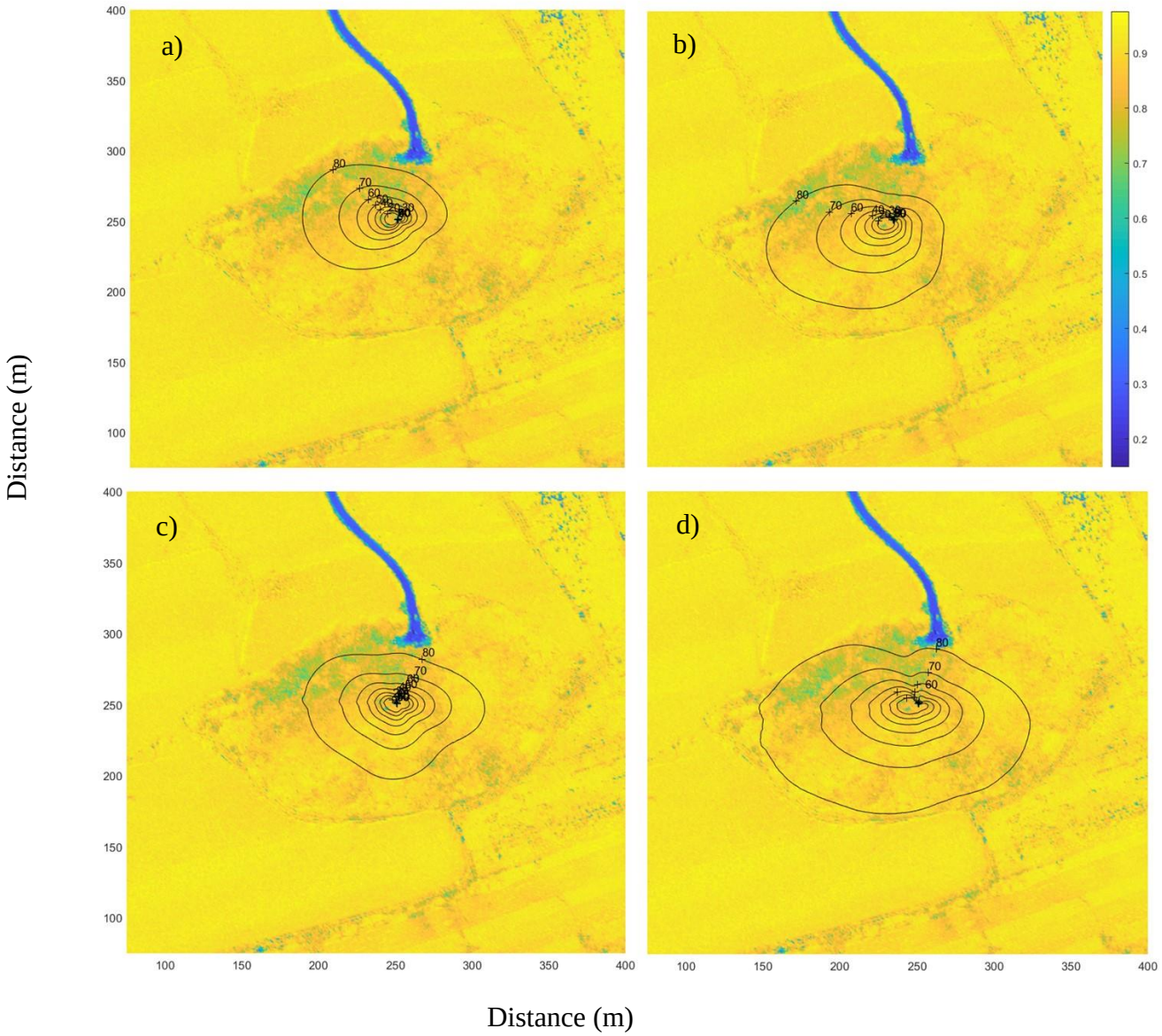

Figure 13. The relative flux contribution for (a) July daytime, (b) July nighttime, (c) October daytime, and (d) October nighttime, overlaying the aerial NDVI values from August 1, 2019. The color legend represents the NDVI readings (ranging from 0.2 to 0.8).

Within the seasonal footprint's boundaries, the NDVI ranged from 0.23 to 0.8, with a mean value of 0.75 from the August 1, 2019 flyover. The NDVI values were consistent across the site, except for low NDVI values in the north portion of the inland salt marsh, shown in green in Figure 13. The variation of the NDVI values could correspond with the differences in vegetation community composition since the plant communities (alvar grassland, Great Lakes dune, inland

salt marsh, and marl fen emergent marsh, and fen) were planted in 2008 in separate plots within the wetland area (Eallonardo, 2010).

For each measurement period, we also calculated the spatially and temporally integrated NDVI that contributed to the half-hour eddy covariance measurement ($NDVI_{fwt}$). The $NDVI_{fwt}$ time-series typically fluctuated between 0.7 and 0.8 (unitless) (Figure 14). The trend seemed more defined in the later months, beginning in September, and continuing through November. The $NDVI_{fwt}$ is calculated based on the NDVI readings from the August 1st flyover and the 30-minute measurements of $wind_{dir}$, $wind_{speed}$, u*, Obukhov atmospheric stability length (L), and crosswind variation (v'v'). A time series of these variables were plotted to understand further the trend present in the $NDVI_{fwt}$ time series (Figure 15). The $wind_{dir}$ time series followed a similar pattern as the $NDVI_{fwt}$ (Figure 15a), indicating that some of the variation of the $NDVI_{fwt}$ time series could be explained by changes in $wind_{dir}$.

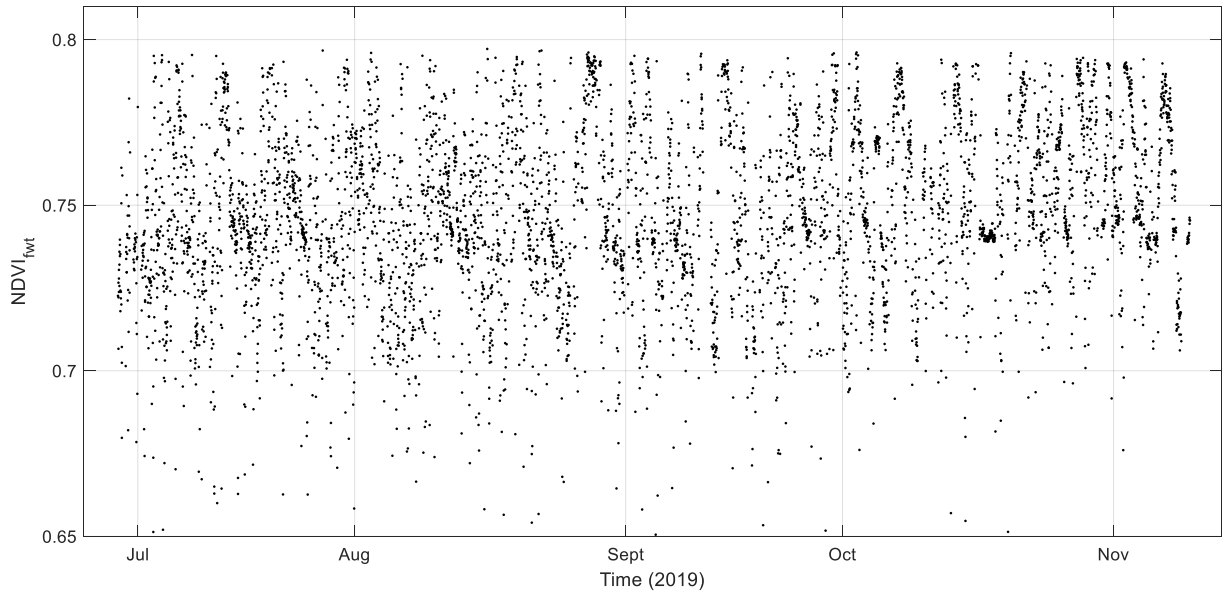

Figure 14. $NDVI_{fwt}$ timeseries, based on the NDVI readings from the August 1st, 2019 flyover within the bounds of the seasonal footprint.

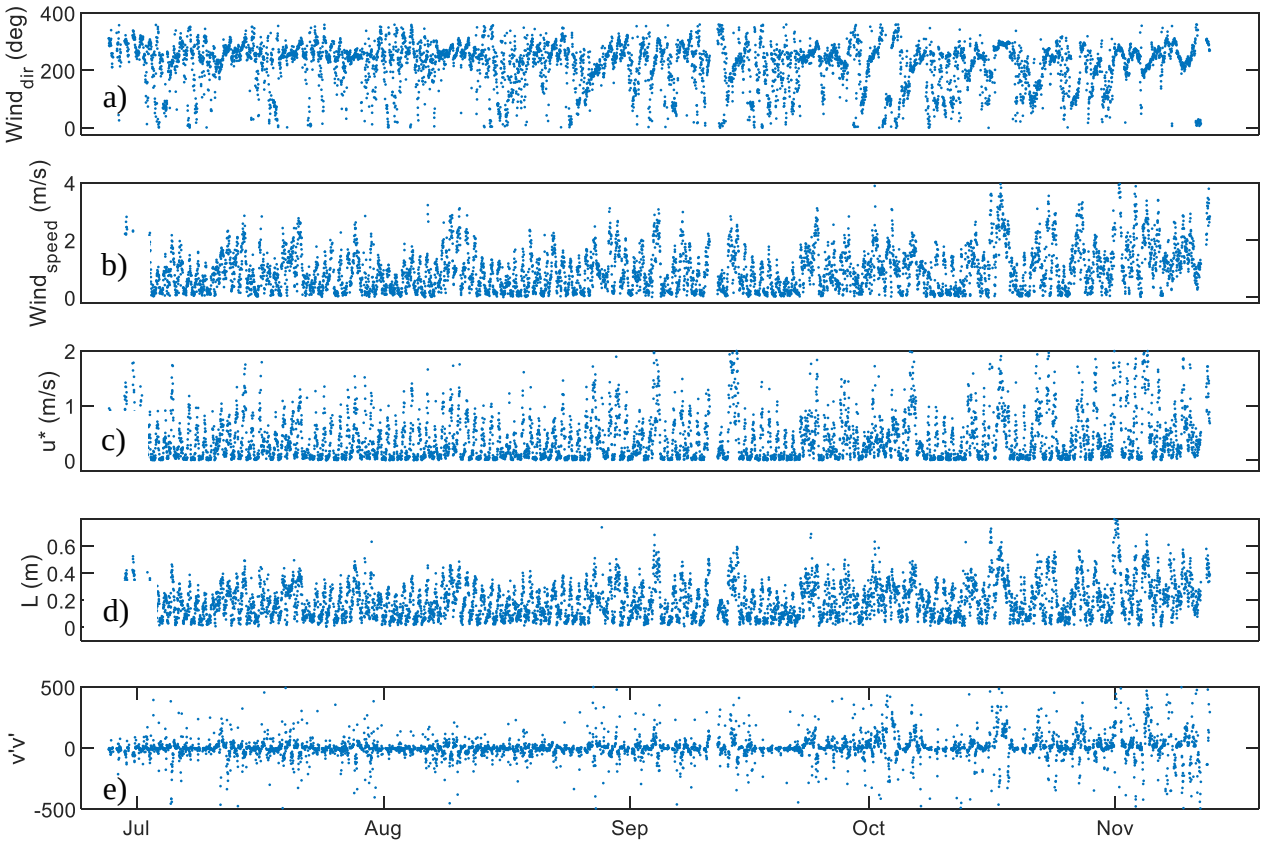

Figure 15. Timeseries of variables that contributed to the footprint. (a) Radial wind direction, (b) wind speed, (c) friction velocity, (d) Obukhov length, and (e) crosswind variance.

As mentioned in section 3.2.2, the stepwise regression models only selected $NDVI_{fwt}$ as a key ecological driver for R_e (Table 7). However, there was no clear relationship determined by the pairwise regression on the half-hour timescale (Figure 12c). Also, we compared each of the carbon fluxes with $NDVI_{fwt}$ on a daily scale to control for temporal dissonance since the time of day may have a strong explanatory effect. The pairwise regression on the daily timescale showed a negative relationship between $NDVI_{fwt}$ and R_e (Figure 16a: $r^2 = 0.03$, $p = 0.032$), which was surprising since a substantial portion of R_e is attributed to plant biomass respiration, which is itself directly driven by the aboveground biomass, and, thus, to NDVI (Gifford, 2003). However,

other factors, like PAR, PPT_T, soil moisture content, vegetation type, and T_{soil} affect both R_e and aboveground production and may overshadow and confound any relationship between NDVI and R_e. Our stepwise regression models had only a limit ability to explore the interaction between variables. Still, they may suggest that the negative correlation between R_e and $NDVI_{fwt}$ could be attributed to the effects of other climatological variables based on the conclusions discussed in Huang et al., (2012) and La Puma et al., (2007), e.g., PAR and VPD.

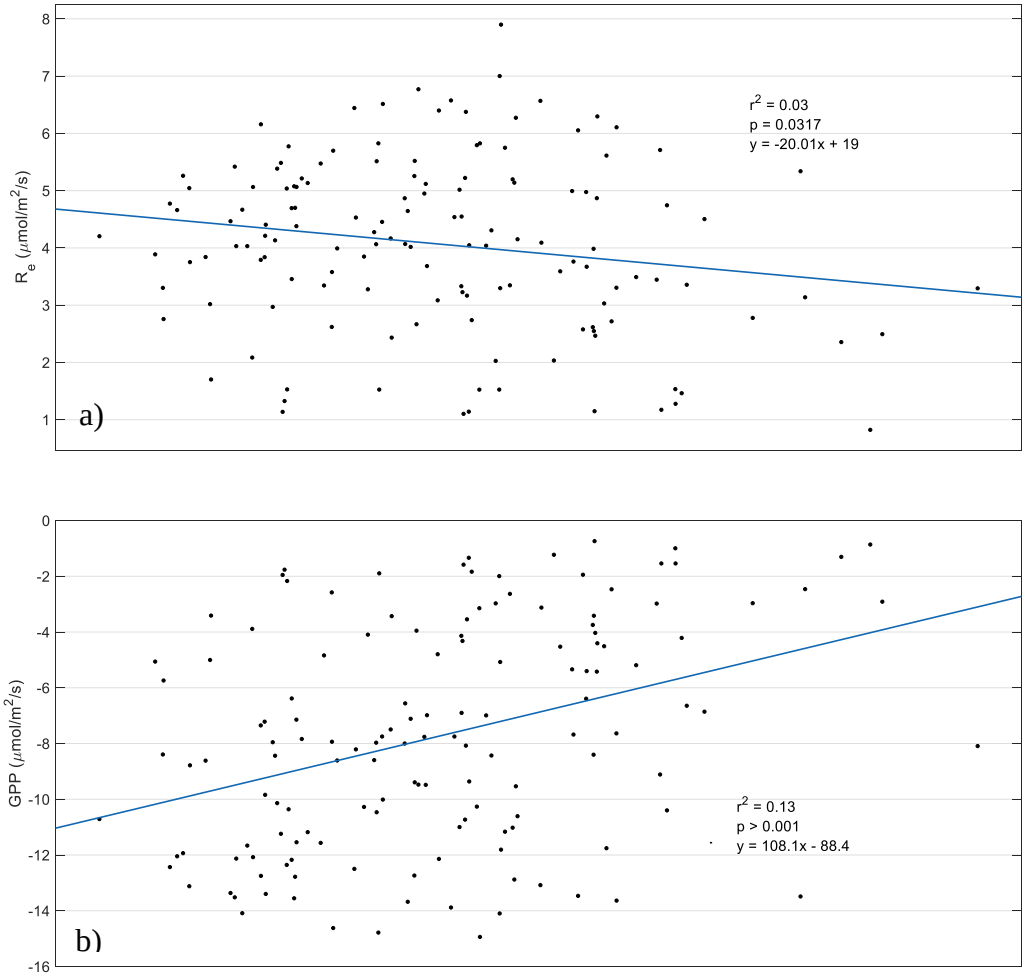

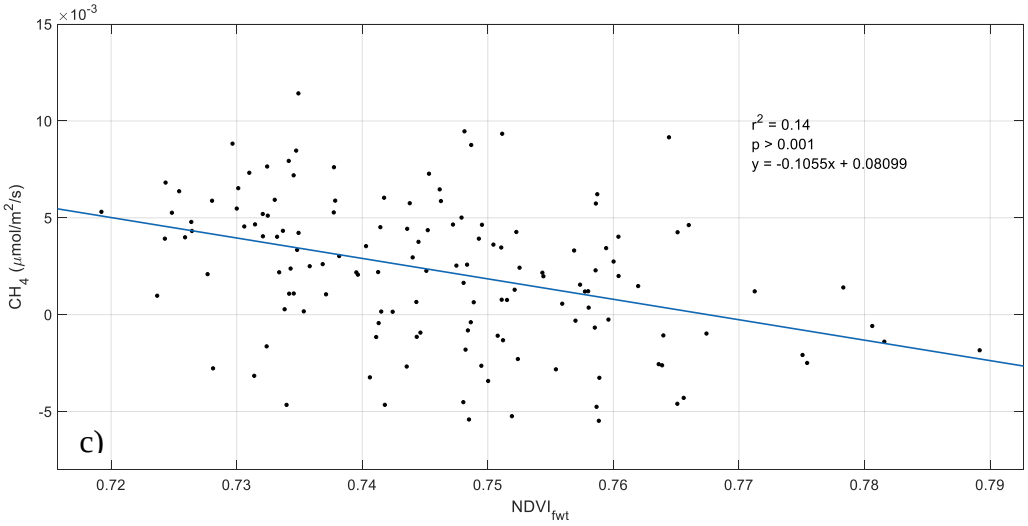

Figure 16. Pairwise relationship between daily averaged $NDVI_{fwt}$ and (a) R_e, (b) GPP, and (c) CH_4. We determined the pairwise regression between the $NDVI_{fwt}$ and the carbon fluxes is best on a daily timescale to eliminate the systematic trends at the half-hour timescale related to the diurnal cycle.

$NDVI_{fwt}$ was selected by the stepwise regression models to influence the CH_4 and GPP fluxes for only some of the months (Table 3 and Table 6), but on a seasonal timescale, the stepwise regression models selected $NDVI_{fwt}$ for GPP and CH_4 fluxes. On the daily timescale the pairwise regression between CH_4 and $NDVI_{fwt}$ showed the best relationship out of the carbon fluxes (Figure 16c: $r^2 = 0.14$, $p < 0.001$), followed by GPP (Figure 16c: $r^2 = 0.13$, $p < 0.001$). The pairwise regression for CH_4 and $NDVI_{fwt}$ showed a negative relationship indicating that areas within the inland salt marsh with lower NDVI values were responsible for an increase in CH_4 fluxes. Conversely, GPP showed a positive relationship. The relationship of $NDVI_{fwt}$ with the carbon fluxes (GPP, R_e, CH_4) was the opposite of what was expected, suggesting that the vegetation's spatial variability of the site may influence the carbon fluxes. Further $NDVI_{fwt}$ readings are required to understand the influence of temporal and spatial variability of phenology and the carbon fluxes at the site.

Chapter 4: Conclusion

This study combined three datasets to assess the empirical drivers of the carbon behavior of an inland salt marsh in Camillus, NY. We found that during the observational period the inland salt-marsh acted as a slight carbon source of 38 $gC \cdot m^2$, including emissions of 9 $gC \cdot m^2$ of CH_4, in CO_2 equivalent, and 29 $gC \cdot m^2$ of CO_2. We attribute the site's small carbon emissions to low CH_4 emissions (mean of 0.0022 $\mu mol \cdot m^{-2} \cdot s^{-1}$), and slight NEE emissions (mean of 0.20 $\mu mol \cdot m^{-2} \cdot s^{-1}$). The cumulative GPP uptake of 566 $gC \cdot m^2$ nearly offset the cumulative R_e emissions of 595 $gC \cdot m^2$. During the growing season, the CH_4 behavior of the site is comparable to saltwater systems, and the CO_2 behavior is on par with other inland marshes. Further observation through the winter and spring would be necessary to make a final determination of the full annual carbon behavior.

The major findings of the study are related to the research objectives outlined below:

Research Objective 1: Determine temporal changes in the statistical relationships between the carbon fluxes and the climatological variables (air temperature, precipitation, vapor pressure density, net radiation, wind speed, wind direction, atmospheric pressure, heat flux, and low friction velocity) and vegetative distribution (NDVI footprint weighted total ($NDVI_{fwt}$)) using an empirical model.

The statistical relationships between the climatological variables and the carbon fluxes changed temporally, however, LE was identified to have a significant explanatory effect for CH_4 and GPP on a monthly and seasonal timescale, while the variation of R_e was best

explained by T_{air}. Both LE and T_{Air} were selected for more than half of the monthly and seasonal stepwise models for all the carbon fluxes, whereas other variables like net_{Rad} and P_a were specific to CH_4 and GPP and were likely attributed to their influence on other critical climatological variables such as LE. These results further illustrate that the carbon fluxes are highly related to LE and T_{Air} and the relationship between the climatological variables themselves.

Research Objective 2: Determine the frequency response of the ecosystem's carbon exchange (CH_4, GPP, R_e) to precipitation events and shifts in atmospheric temperature during the growing season.

CH_4, GPP, and R_e all showed significant lag responses to T_{air} and PPT_T. However, the lag responses of CH_4 (5-hours) and R_e (3-hours) from T_{Air}, we attribute to the lag response between T_{Air} and T_{Soil} rather than between T_{Air} and the carbon fluxes themselves. CH_4 showed the longest lag response to PPT_T of one-day that we attribute to the time it takes for the increased DO concentrations from PPT_T events to reduce to anoxic conditions, versus GPP and R_e, which showed a 1-hour and 2-hour lag response to rain events. The fast reaction from GPP to PPT_T is like an indicator of a water limitation at the site throughout the growing season and an immediate increase in DO within the water table.

Research Objective 3: Evaluate the spatial influence of a heterogeneous plant community from an individual NDVI event on site-level integrated carbon fluxes.

Surprisingly, R_e was the only carbon flux that $NDVI_{fwt}$ was identified to have a significant explanatory effect for more than half of the months and the season. The pairwise regression on a daily timescale indicated that land-cover heterogeneity ($NDVI_{fwt}$) showed to have a slight positive relationship with GPP, and a negative relationship with CH_4 and R_e, all of which were the opposite of what we hypothesized. The NDVI values within the footprint contribution had a low variation, values fluctuated between 0.7 and 0.8, with a mean NDVI of 0.75. The low variability of the $NDVI_{fwt}$ proposed a limitation for fine-scale analysis, likely contributing to the negative results. Additional NDVI readings are necessary to assess how the heterogeneity of the site influenced carbon behavior.

4.1 Future Direction

This study provides an analysis of the site-specific carbon flux empirical drivers at an inland salt marsh in Camillus, NY. There are many potential steps forward, including:

1) Expand analysis to include a comparison of the carbon fluxes captured at the inland salt marsh during this observational study and the carbon fluxes obtained during the water budget assessment conducted by O'Brien and Gere from April 2011 to December 2011 and April 2012 to May 2013.
2) Expand the observational period through winters to capture the carbon behavior during an annual timescale.
3) Further investigate the relationship between the NDVI values and the carbon fluxes of the site by conducting an additional observational study that includes monthly NDVI

readings, continuous measurement of the carbon fluxes, and a field survey of the present plant communities.

4) Utilize the data from Ameriflux to assess site-specific empirical drivers and to determine common drivers among the sites, including other ecosystems (e.g., forested, or tidal systems).
5) Determine a complete water budget of the inland salt marsh, including the measurement of unsaturated and saturated zones based on PPT_T events.

References

Admiraal, W.: Influence of light and temperature on the growth rate of estuarine benthic diatoms in culture, Mar. Biol., 39(1), 1–9, 1976.

Admiraal, W.: Tolerance of estuarine benthic diatoms to high concentrations of ammonia, nitrite ion, nitrate ion and orthophosphate, Mar. Biol., 43(4), 307–315, doi:10.1007/BF00396925, 1977.

Aerts, R.: Climate, leaf litter chemistry and leaf litter decomposition in terrestrial ecosystems: a triangular relationship, Oikos, 439–449, 1997.

Alford, D. P., Delaune, R. D. and Lindau, C. W.: Methane flux from Missippi River deltaic plain wetlands, Biogeochemistry, 37(3), 227–236, 1997.

Aurela, M., Riutta, T., Laurila, T., Tuovinen, J.-P., Vesala, T., Tuittila, E.-S., Rinne, J., Haapanala, S. and Laine, J.: CO_2 exchange of a sedge fen in southern Finland-the impact of a drought period, Tellus B Chem. Phys. Meteorol., 59(5), 826–837, doi:10.1111/j.1600-0889.2007.00309.x, 2007.

Bahn, M., Janssens, I. A., Reichstein, M., Smith, P. and Trumbore, S. E.: Soil respiration across scales: towards an integration of patterns and processes: Meetings, New Phytol., 186(2), 292–296, doi:10.1111/j.1469-8137.2010.03237.x, 2010.

Baker, I., Denning, A. S., Hanan, N., Prihodko, L., Uliasz, M., Vidale, P., Davis, K. and Bakwin, P.: Simulated and observed fluxes of sensible and latent heat and CO2 at the WLEF-TV tower using SiB2. 5, Glob. Change Biol., 9(9), 1262–1277, 2003.

Baldocchi, D.: Assessing the eddy covariance technique for evaluating carbon dioxide exchange rates of ecosystems: Past, present and future., 2003.

Baldocchi, D., Falge, E., Gu, L., Olson, R., Hollinger, D., Running, S., Anthoni, P., Bernhofer, C., Davis, K. and Evans, R.: FLUXNET: A new tool to study the temporal and spatial variability of ecosystem-scale carbon dioxide, water vapor, and energy flux densities, Bull. Am. Meteorol. Soc., 82(11), 2415–2434, 2001.

Ball, J. T., Woodrow, I. E. and Berry, J. A.: A Model Predicting Stomatal Conductance and its Contribution to the Control of Photosynthesis under Different Environmental Conditions, in Progress in Photosynthesis Research, edited by J. Biggins, pp. 221–224, Springer Netherlands, Dordrecht., 1987.

Binghamton, NY Weather Forecast Office: Syracuse Annual Climate Summary, Climatological Report, National Weather Service., 2020.

Binkley, D., Stape, J. L., Takahashi, E. N. and Ryan, M. G.: Tree-girdling to separate root and heterotrophic respiration in two Eucalyptus stands in Brazil, Oecologia, 148(3), 447–454, doi:10.1007/s00442-006-0383-6, 2006.

Birch, H.: Further observations on humus decomposition and nitrification, Plant Soil, 262–286, 1959.

Bloom, A. A., Palmer, P. I., Fraser, A., Reay, D. S. and Frankenberg, C.: Large-scale controls of methanogenesis inferred from methane and gravity spaceborne data, Science, 327(5963), 322–325, 2010.

Boelman, N. T., Stieglitz, M., Rueth, H. M., Sommerkorn, M., Griffin, K. L., Shaver, G. R. and Gamon, J. A.: Response of NDVI, biomass, and ecosystem gas exchange to long-term warming and fertilization in wet sedge tundra, Oecologia, 135(3), 414–421, doi:10.1007/s00442-003-1198-3, 2003.

Bohn, T. J., Lettenmaier, D. P., Sathulur, K., Bowling, L. C., Podest, E., McDonald, K. C. and Friborg, T.: Methane emissions from western Siberian wetlands: heterogeneity and sensitivity to climate change, Environ. Res. Lett., 2(4), 045015, doi:10.1088/1748-9326/2/4/045015, 2007.

Bond-Lamberty, B., Wang, C. and Gower, S. T.: A global relationship between the heterotrophic and autotrophic components of soil respiration?, Glob. Change Biol., 10(10), 1756–1766, 2004.

Boon, P. I.: Carbon cycling in Australian wetlands: the importance of methane, SIL Proc. 1922-2010, 27(1), 37–50, doi:10.1080/03680770.1998.11901202, 2000.

Bridgham, S. D., Megonigal, J. P., Keller, J. K., Bliss, N. B. and Trettin, C.: The carbon balance of North American wetlands, Wetlands, 26(4), 889–916, doi:10.1672/0277-5212(2006)26[889:TCBONA]2.0.CO;2, 2006.

Chamberlain, S., Silver, W. L., Anthony, T., Hemes, K. S., Oikawa, P., Sturtevant, C., Eichelmann, E., Matthes, J. H., Verfaillie, J. G. and Baldocchi, D. D.: Identifying drivers of divergent methane fluxes from restored wetlands, AGU Fall Meet. Abstr., 52 [online] Available from: http://adsabs.harvard.edu/abs/2017AGUFM.B52C..02C (Accessed 26 September 2018), 2017.

Chu, H., Chen, J., Gottgens, J. F., Ouyang, Z., John, R., Czajkowski, K. and Becker, R.: Net ecosystem methane and carbon dioxide exchanges in a Lake Erie coastal marsh and a nearby cropland: CH4 and CO2 fluxes in a freshwater marsh, J. Geophys. Res. Biogeosciences, 119(5), 722–740, doi:10.1002/2013JG002520, 2014.

Colijn, F. and Van Buurt, G.: Influence of light and temperature on the photosynthetic rate of marine benthic diatoms, Mar. Biol., 31(3), 209–214, 1975.

Davidson, E. A. and Janssens, I. A.: Temperature sensitivity of soil carbon decomposition and feedbacks to climate change, Nature, 440(7081), 165–173, 2006.

Detto, M., Montaldo, N., Albertson, J. D., Mancini, M. and Katul, G.: Soil moisture and vegetation controls on evapotranspiration in a heterogeneous Mediterranean ecosystem on Sardinia, Italy, Water Resour. Res., 42(8), 2006.

Eallonardo, A. S.: Inland salt marsh ecology and the restoration of rare plant communities on a Solvay waste site : a functional approach, State University of New York, College of Environmental Science and Forestry, Syracuse, NY., 2010.

Edenhofer, O.: Climate change 2014: mitigation of climate change, Cambridge University Press., 2015.

Farmer, D. K., Wooldridge, P. J. and Cohen, R. C.: Application of thermal-dissociation laser induced fluorescence (TD-LIF) to measurement of HNO_3, Σalkyl nitrates, Σperoxy nitrates, and NO_2 fluxes using eddy covariance, Atmospheric Chem. Phys., 6(11), 3471–3486, doi:10.5194/acp-6-3471-2006, 2006.

Ford, H., Garbutt, A., Jones, L. and Jones, D. L.: Methane, carbon dioxide and nitrous oxide fluxes from a temperate salt marsh: Grazing management does not alter Global Warming Potential, Estuar. Coast. Shelf Sci., 113, 182–191, doi:10.1016/j.ecss.2012.08.002, 2012.

Frolking, S. E., Bubier, J. L., Moore, T. R., Ball, T., Bellisario, L. M., Bhardwaj, A., Carroll, P., Crill, P. M., Lafleur, P. M., McCaughey, J. H., Roulet, N. T., Suyker, A. E., Verma, S. B., Waddington, J. M. and Whiting, G. J.: Relationship between ecosystem productivity and photosynthetically active radiation for northern peatlands, Glob. Biogeochem. Cycles, 12(1), 115–126, doi:10.1029/97GB03367, 1998.

Froment, A.: Soil Respiration in a Mixed Oak Forest, Oikos, 23(2), 273, doi:10.2307/3543417, 1972.

Gifford, R. M.: Plant respiration in productivity models: conceptualisation, representation and issues for global terrestrial carbon-cycle research, Funct. Plant Biol., 30(2), 171, doi:10.1071/FP02083, 2003.

Goward, S. N., Tucker, C. J. and Dye, D. G.: North American vegetation patterns observed with the NOAA-7 advanced very high resolution radiometer, Vegetatio, 64(1), 3–14, doi:10.1007/BF00033449, 1985.

Granger, C. W.: Investigating causal relations by econometric models and cross-spectral methods, Econom. J. Econom. Soc., 424–438, 1969.

Hao, Y. B., Cui, X. Y., Wang, Y. F., Mei, X. R., Kang, X. M., Wu, N., Luo, P. and Zhu, D.: Predominance of Precipitation and Temperature Controls on Ecosystem CO2 Exchange in Zoige Alpine Wetlands of Southwest China, Wetlands, 31(2), 413–422, doi:10.1007/s13157-011-0151-1, 2011.

Hewlett, J. D.: The development of vegetation on the Solvay waste beds, 1956.

Hinojo-Hinojo, C., Castellanos, A. E., Rodriguez, J. C., Delgado-Balbuena, J., Romo-León, J. R., Celaya-Michel, H. and Huxman, T. E.: Carbon and Water Fluxes in an Exotic Buffelgrass Savanna, Rangel. Ecol. Manag., 69(5), 334–341, doi:10.1016/j.rama.2016.04.002, 2016.

Hoff, J. H.: Lectures on Theoretical and Physical Chemistry: Chemical dynamics, Arnold. [online] Available from: https://books.google.com/books?id=hx0dnAEACAAJ, 1898.

Hofstra, G. and Hesketh, J. D.: The effect of temperature on stomatal aperture in different species, Can. J. Bot., 47(8), 1307–1310, doi:10.1139/b69-184, 1969.

Hopkins, F., Gonzalez-Meler, M. A., Flower, C. E., Lynch, D. J., Czimczik, C., Tang, J. and Subke, J.: Ecosystem-level controls on root-rhizosphere respiration, New Phytol., 199(2), 339–351, 2013.

Hsieh, C.-I., Katul, G. and Chi, T.: An approximate analytical model for footprint estimation of scalar fluxes in thermally stratified atmospheric flows, Adv. Water Resour., 23(7), 765–772, 2000.

Huang, N., Niu, Z., Zhan, Y., Xu, S., Tappert, M. C., Wu, C., Huang, W., Gao, S., Hou, X. and Cai, D.: Relationships between soil respiration and photosynthesis-related spectral vegetation indices in two cropland ecosystems, Agric. For. Meteorol., 160, 80–89, doi:10.1016/j.agrformet.2012.03.005, 2012.

Inglett, K. S., Inglett, P. W., Reddy, K. R. and Osborne, T. Z.: Temperature sensitivity of greenhouse gas production in wetland soils of different vegetation, Biogeochemistry, 108(1), 77–90, doi:10.1007/s10533-011-9573-3, 2012.

Intergovernmental Panel on Climate Change and Edenhofer, O., Eds.: Climate change 2014: mitigation of climate change: Working Group III contribution to the Fifth Assessment Report of the Intergovernmental Panel on Climate Change, Cambridge University Press, New York, NY., 2014.

Jeong, S.-H., Eom, J.-Y., Park, J.-Y., Chun, J.-H. and Lee, J.-S.: Effect of precipitation on soil respiration in a temperate broad-leaved forest, J. Ecol. Environ., 42(1), 10, doi:10.1186/s41610-018-0071-6, 2018.

Johnson, L. C., Shaver, G. R., Cades, D. H., Rastetter, E., Nadelhoffer, K., Giblin, A., Laundre, J. and Stanley, A.: Plant Carbon–Nutrient Interactions Control Co $_2$ Exchange In Alaskan Wet Sedge Tundra Ecosystems, Ecology, 81(2), 453–469, doi:10.1890/0012-9658(2000)081[0453:PCNICC]2.0.CO;2, 2000.

Kaimal, J. C. and Gaynor, J. E.: Another look at sonic thermometry, Bound.-Layer Meteorol., 56(4), 401–410, doi:10.1007/BF00119215, 1991.

Kathilankal, J. C., Mozdzer, T. J., Fuentes, J. D., D'Odorico, P., McGlathery, K. J. and Zieman, J. C.: Tidal influences on carbon assimilation by a salt marsh, Environ. Res. Lett., 3(4), 044010, doi:10.1088/1748-9326/3/4/044010, 2008.

Kieft, T. L.: Microbial biomass response to a rapid increase in water potential when dry soil is wetted, Soil Biol. Biochem., 19(2), 119–126, 1987.

Kim, J., Verma, S. B., Billesbach, D. P. and Clement, R. J.: Diel variation in methane emission from a midlatitude prairie wetland: Significance of convective throughflow in *Phragmites australis*, J. Geophys. Res. Atmospheres, 103(D21), 28029–28039, doi:10.1029/98JD02441, 1998.

Kirschke, S., Bousquet, P., Ciais, P., Saunois, M., Canadell, J. G., Dlugokencky, E. J., Bergamaschi, P., Bergmann, D., Blake, D. R. and Bruhwiler, L.: Three decades of global methane sources and sinks, Nat. Geosci., 6(10), 813–823, 2013.

Kumar, M. and Monteith, J.: Remote sensing of crop growth. In: Smith (ed) Plants and the daylight spectrum., Academic PRess, 133–144, 1981.

La Puma, I. P., Philippi, T. E. and Oberbauer, S. F.: Relating NDVI to ecosystem CO2 exchange patterns in response to season length and soil warming manipulations in arctic Alaska, Remote Sens. Environ., 109(2), 225–236, doi:10.1016/j.rse.2007.01.001, 2007.

Lafleur, P. M., Roulet, N. T. and Admiral, S. W.: Annual cycle of CO_2 exchange at a bog peatland, J. Geophys. Res. Atmospheres, 106(D3), 3071–3081, doi:10.1029/2000JD900588, 2001.

Lee, R.: Forest microclimatology, Columbia University Press, New York., 1978.

Lee, X., Massman, W. and Law, B.: Handbook of Micrometeorology: A Guide for Surface Flux Measurement and Analysis, vol. 29., 2004.

LI-COR Biosciences: LI-7500RS Open Path CO2/H2O Gas Analyzer Instruction Manual, [online] Available from: https://www.licor.com/documents/c7tyf0czqn9ezkq1ki3b, 2019.

LI-COR Biosciences: LI-7700 Open Path CH4 Gas Analyzer Instruction Manual, [online] Available from: https://www.licor.com/documents/18warrx05laaa1zo9s0pepmjk0cgiqm3, 2020.

Lloyd, J. and Taylor, J. A.: On the Temperature Dependence of Soil Respiration, Funct. Ecol., 8(3), 315, doi:10.2307/2389824, 1994.

Lu, W., Xiao, J., Liu, F., Zhang, Y., Liu, C. and Lin, G.: Contrasting ecosystem CO_2 fluxes of inland and coastal wetlands: a meta-analysis of eddy covariance data, Glob. Change Biol., 23(3), 1180–1198, doi:10.1111/gcb.13424, 2017.

Lund, M., Lafleur, P. M., Roulet, N. T., Lindroth, A., Christensen, T. R., Aurela, M., Chojnicki, B. H., Flanagan, L. B., Humphreys, E. R., Laurila, T., Oechel, W. C., Olejnik, J., Rinne, J., Schubert, P. and Nilsson, M. B.: Variability in exchange of CO2 across 12 northern peatland and tundra sites: Exchange Of Co2 In Wetlands, Glob. Change Biol., no-no, doi:10.1111/j.1365-2486.2009.02104.x, 2009.

Massman, W. J.: A simple method for estimating frequency response corrections for eddy covariance systems, Agric. For. Meteorol., 104(3), 185–198, doi:10.1016/S0168-1923(00)00164-7, 2000.

Meentemeyer, V.: The geography of organic decomposition rates, Ann. Assoc. Am. Geogr., 74(4), 551–560, 1984.

Mirck, J. and Volk, T. A.: Response of three shrub willow varieties (Salix spp.) to storm water treatments with different concentrations of salts, Bioresour. Technol., 101(10), 3484–3492, 2010.

Morin, T. H., Bohrer, G., Frasson, R. P. d M., Naor-Azreli, L., Mesi, S., Stefanik, K. C. and Schäfer, K. V. R.: Environmental drivers of methane fluxes from an urban temperate wetland park, J. Geophys. Res. Biogeosciences, 119(11), 2188–2208, doi:10.1002/2014JG002750, 2014a.

Morin, T. H., Bohrer, G., Naor-Azrieli, L., Mesi, S., Kenny, W. T., Mitsch, W. J. and Schäfer, K. V. R.: The seasonal and diurnal dynamics of methane flux at a created urban wetland, Ecol. Eng., 72, 74–83, doi:10.1016/j.ecoleng.2014.02.002, 2014b.

Neubauer, S. C.: Ecosystem Responses of a Tidal Freshwater Marsh Experiencing Saltwater Intrusion and Altered Hydrology, Estuaries Coasts, 36(3), 491–507, doi:10.1007/s12237-011-9455-x, 2013.

New York State Department of Environmental Conservation: Consent order, Index No. D-7-0001-02-03 ,Site No. 7-34-076 (Solvay Wastebeds 9-15)., 2010.

Niu, S., Luo, Y., Fei, S., Yuan, W., Schimel, D., Law, B. E., Ammann, C., Altaf Arain, M., Arneth, A., Aubinet, M., Barr, A., Beringer, J., Bernhofer, C., Andrew Black, T., Buchmann, N., Cescatti, A., Chen, J., Davis, K. J., Dellwik, E., Desai, A. R., Etzold, S., Francois, L., Gianelle, D., Gielen, B., Goldstein, A., Groenendijk, M., Gu, L., Hanan, N., Helfter, C., Hirano, T., Hollinger, D. Y., Jones, M. B., Kiely, G., Kolb, T. E., Kutsch, W. L., Lafleur, P., Lawrence, D. M., Li, L., Lindroth, A., Litvak, M., Loustau, D., Lund, M., Marek, M., Martin, T. A., Matteucci, G., Migliavacca, M., Montagnani, L., Moors, E., William Munger, J., Noormets, A., Oechel, W., Olejnik, J., U, K. T. P., Pilegaard, K., Rambal, S., Raschi, A., Scott, R. L., Seufert, G., Spano, D., Stoy, P., Sutton, M. A., Varlagin, A., Vesala, T., Weng, E., Wohlfahrt, G., Yang, B., Zhang, Z. and Zhou, X.: Thermal optimality of net ecosystem exchange of carbon dioxide and underlying mechanisms, New Phytol., 194(3), 775–783, doi:10.1111/j.1469-8137.2012.04095.x, 2012.

Ortiz-Llorente, M. J. and Alvarez-Cobelas, M.: Comparison of biogenic methane emissions from unmanaged estuaries, lakes, oceans, rivers and wetlands, Atmos. Environ., 59, 328–337, doi:10.1016/j.atmosenv.2012.05.031, 2012.

Penman, H. L.: Natural evaporation from open water, bare soil and grass, Proc. R. Soc. Lond. Ser. Math. Phys. Sci., 193(1032), 120–145, doi:10.1098/rspa.1948.0037, 1948.

Piao, S., Fang, J., Ciais, P., Peylin, P., Huang, Y., Sitch, S. and Wang, T.: The carbon balance of terrestrial ecosystems in China., 2009.

Priestley, C. H. B.: Atmospheric Pressure Changes, Nature, 158(4025), 914–914, doi:10.1038/158914a0, 1946.

Raich, J. W. and Schlesinger, W. H.: The global carbon dioxide flux in soil respiration and its relationship to vegetation and climate, Tellus B Chem. Phys. Meteorol., 44(2), 81–99, doi:10.3402/tellusb.v44i2.15428, 1992.

Reichstein, M., Falge, E., Baldocchi, D., Papale, D., Aubinet, M., Berbigier, P., Bernhofer, C., Buchmann, N., Gilmanov, T. and Granier, A.: On the separation of net ecosystem exchange into assimilation and ecosystem respiration: review and improved algorithm, Glob. Change Biol., 11(9), 1424–1439, 2005.

Reid, M. C., Tripathee, R., Schäfer, K. V. R. and Jaffé, P. R.: Tidal marsh methane dynamics: Difference in seasonal lags in emissions driven by storage in vegetated versus unvegetated sediments: Tidal Marsh Methane Dynamics, J. Geophys. Res. Biogeosciences, 118(4), 1802–1813, doi:10.1002/2013JG002438, 2013.

Rey-Sanchez, A. C., Morin, T. H., Stefanik, K. C., Wrighton, K. and Bohrer, G.: Determining total emissions and environmental drivers of methane flux in a Lake Erie estuarine marsh, Ecol. Eng., 114, 7–15, doi:10.1016/j.ecoleng.2017.06.042, 2018.

Rinne, J., Riutta, T., Pihlatie, M., Aurela, M., Haapanala, S., Tuovinen, J.-P., Tuittila, E.-S. and Vesala, T.: Annual cycle of methane emission from a boreal fen measured by the eddy covariance technique, Tellus B Chem. Phys. Meteorol., 59(3), 449–457, doi:10.1111/j.1600-0889.2007.00261.x, 2007.

Rinne, J., Tuittila, E.-S., Peltola, O., Li, X., Raivonen, M., Alekseychik, P., Haapanala, S., Pihlatie, M., Aurela, M., Mammarella, I. and Vesala, T.: Temporal Variation of Ecosystem Scale Methane Emission From a Boreal Fen in Relation to Temperature, Water Table Position, and Carbon Dioxide Fluxes, Glob. Biogeochem. Cycles, 32(7), 1087–1106, doi:10.1029/2017GB005747, 2018.

Roulet, N. T.: Peatlands, carbon storage, greenhouse gases, and the Kyoto Protocol: Prospects and significance for Canada, Wetlands, 20(4), 605–615, doi:10.1672/0277-5212(2000)020[0605:PCSGGA]2.0.CO;2, 2000.

Schäfer, K. V. R., Tripathee, R., Artigas, F., Morin, T. H. and Bohrer, G.: Carbon dioxide fluxes of an urban tidal marsh in the Hudson-Raritan estuary: Carbon dioxide fluxes of an wetland, J. Geophys. Res. Biogeosciences, 119(11), 2065–2081, doi:10.1002/2014JG002703, 2014.

Schedlbauer, J. L., Munyon, J. W., Oberbauer, S. F., Gaiser, E. E. and Starr, G.: Controls on Ecosystem Carbon Dioxide Exchange in Short- and Long-Hydroperiod Florida Everglades Freshwater Marshes, Wetlands, 32(5), 801–812, doi:10.1007/s13157-012-0311-y, 2012.

Schmid, H. P.: Source areas for scalars and scalar fluxes, Bound.-Layer Meteorol., 67(3), 293–318, doi:10.1007/BF00713146, 1994.

Sellers, P. J.: Canopy reflectance, photosynthesis, and transpiration, II. The role of biophysics in the linearity of their interdependence, Remote Sens. Environ., 21(2), 143–183, doi:10.1016/0034-4257(87)90051-4, 1987.

Sha, C., Mitsch, W. J., Mander, Ü., Lu, J., Batson, J., Zhang, L. and He, W.: Methane emissions from freshwater riverine wetlands, Ecol. Eng., 37(1), 16–24, doi:10.1016/j.ecoleng.2010.07.022, 2011.

Singh, J. S. and Gupta, S. R.: Plant decomposition and soil respiration in terrestrial ecosystems, Bot. Rev., 43(4), 449–528, doi:10.1007/BF02860844, 1977.

Sollid, J. L. and Sørbel, L.: Palsa Bogs as a Climate Indicator: Examples from Dovrefjell, Southern Norway, Ambio, 27(4), 287–291, 1998.

Sturtevant, C., Ruddell, B. L., Knox, S. H., Verfaillie, J., Matthes, J. H., Oikawa, P. Y. and Baldocchi, D.: Identifying scale-emergent, nonlinear, asynchronous processes of wetland methane exchange: Identifying Methane Exchange Processes, J. Geophys. Res. Biogeosciences, 121(1), 188–204, doi:10.1002/2015JG003054, 2016.

Teskey, R. O., Saveyn, A., Steppe, K. and McGuire, M. A.: Origin, fate and significance of CO_2 in tree stems, New Phytol., 0(0), 071120093824001-???, doi:10.1111/j.1469-8137.2007.02286.x, 2007.

Tokida, T., Miyazaki, T., Mizoguchi, M., Nagata, O., Takakai, F., Kagemoto, A. and Hatano, R.: Falling atmospheric pressure as a trigger for methane ebullition from peatland, Glob. Biogeochem. Cycles, 21(2), 2007.

Trumbore, S.: Carbon respired by terrestrial ecosystems–recent progress and challenges, Glob. Change Biol., 12(2), 141–153, 2006.

Tucker, C. J.: Red and photographic infrared linear combinations for monitoring vegetation, Remote Sens. Environ., 8(2), 127–150, doi:10.1016/0034-4257(79)90013-0, 1979.

Wang, K., Liu, C., Zheng, X., Pihlatie, M., Li, B., Haapanala, S., Vesala, T., Liu, H., Wang, Y., Liu, G. and Hu, F.: Comparison between eddy covariance and automatic chamber techniques for measuring net ecosystem exchange of carbon dioxide in cotton and wheat fields, , 13, 2013.

Waring, R., Landsberg, J. and Williams, M.: Net primary production of forests: a constant fraction of gross primary production?, Tree Physiol., 18(2), 129–134, 1998.

Webb, E. K., Pearman, G. I. and Leuning, R.: Correction of flux measurements for density effects due to heat and water vapour transfer, Q. J. R. Meteorol. Soc., 106(447), 85–100, 1980.

Witkamp, M.: Decomposition of Leaf Litter in Relation to Environment, Microflora, and Microbial Respiration, Ecology, 47(2), 194–201, doi:10.2307/1933765, 1966.

Wolfe, G. M., Thornton, J. A., Yatavelli, R. L. N., McKay, M., Goldstein, A. H., LaFranchi, B., Min, K.-E. and Cohen, R. C.: Eddy covariance fluxes of acyl peroxy nitrates (PAN, PPN and MPAN) above a Ponderosa pine forest, Atmospheric Chem. Phys., 9(2), 615–634, doi:10.5194/acp-9-615-2009, 2009.

Xiao, J. and Moody, A.: Geographical distribution of global greening trends and their climatic correlates: 1982–1998, Int. J. Remote Sens., 26(11), 2371–2390, 2005.

Zedler, J. B. and Kercher, S.: WETLAND RESOURCES: Status, Trends, Ecosystem Services, and Restorability, Annu. Rev. Environ. Resour., 30(1), 39–74, doi:10.1146/annurev.energy.30.050504.144248, 2005.

Zhou, L., Zhou, G. and Jia, Q.: Annual cycle of CO2 exchange over a reed (Phragmites australis) wetland in Northeast China, Aquat. Bot., 91(2), 91–98, doi:10.1016/j.aquabot.2009.03.002, 2009.

Vitae

Veronica Davies

+1 856 470 0072 • Veronica.L.Davies@gmail.com

EDUCATION

State University of New York College of Environmental Science and Forestry | Syracuse, NY

Master's Degree in Ecological Engineering, GPA 3.87 08/2018 – 08/2020

Rutgers, The State University of New Jersey | New Brunswick, NJ

Bachelor's Degree in Bioenvironmental Engineering, GPA 3.29 09/2013 – 01/2016

WORK EXPERIENCE

State University of New York College of Environmental Science and Forestry | Syracuse, NY

Graduate Research Assistant 05/2019 – present

- Designed, sourced parts for, installed & maintained an eddy-covariance tower to capture carbon fluxes.
- Drafted and built closed flux chambers to determine greenhouse gas transfer through macrophytes.
- Assessed the ecological drivers of methane & carbon dioxide fluxes using an empirical model in MATLAB.

Graduate Teaching Assistant 08/2018 – 05/2019

- Guest lectured 40+ students; developed homework assignments and held weekly office hours.

Engineers without Borders, Syracuse Professional Chapter | Syracuse, NY

Water Quality Group Co-lead (Volunteer) 09/2018 – present

- Delegated and reviewed water disinfection engineering solutions for the implementation of a drinking water supply for a village of 500 families in Las Majadas and Bella Vista, Guatemala; corresponded regularly with Guatemalan project contacts about construction status and water quality reports and standards.

New Jersey Department of Environmental Protection | Trenton, NJ

Environmental Engineer 04/2016 – 07/2018

- Reviewed environmental permit applications for regulatory applicability and issued final action documents.

- Collaborated with stakeholders, USEPA and NJDEP programs on air quality permit development, regulatory changes, and public comment response documents.

Municipal Public Access Planning Project Manager 08/2015 – 03/2016

- Drafted Municipal Public Access Plans including field observations, ArcGIS maps and compliance review.
- Updated NJDEP's inventory post hurricane Sandy of public access locations to tidally influenced waterways through visual site assessments using Collector for ArcGIS.

Coastal Management Intern 06/2015 – 08/2015

- Conducted literature review on how living shorelines are defined, regulated, and incentivized; identified possible living shoreline locations using ArcGIS, relevant databases, and living shoreline engineering guidelines.

CERTIFICATIONS & TRAINING

- Pathways to Net-Zero Carbon, SUNY ESF, Jan. 2020 – May 2020
- Climate Change Adaptation and Mitigation Program Development, SUNY ESF, Aug. 2019 - Dec. 2019
- Certified Professional in Erosion and Sediment Control - IT, EnviroCert International, Inc., Mar. 2019
- Air Toxics Training, US Environmental Protection Agency Region 1, May 2017
- APTI 452 Principles and Practices of Air Pollution Training, Rutgers University, Jun. 2016
- ArcGIS Workshop, New Jersey Department of Environmental Protection, Aug. 2015
- Living Shoreline Marine Contractor Training, Partnership for the Delaware Estuary, Jun. 2015
- 40-Hr. HAZWOPER Certification, Rutgers University, Dec. 2014

AWARDS

- North American Carbon Program Travel Award, $500
- OIGS Graduate Student Travel Grant, $300
- O'Brien and Gere Graduate Fellowship, $1,000

PRESENTATIONS

Davies, V., Morin, T., & Volk, T. (2020). *Characterization of the empirical drivers of the carbon budget of a constructed inland salt marsh*. Poster session presented at the annual meeting of the American Ecological Engineering Society.

Brazier, F., Daley, E., Davies, V., Fennell, Dr. D., Rattana, S., Reichard, M., Peloski, A., (2015) *Microbial Bio-dechlorination of TCE in Soils from the Rutgers University Campuses*. Poster session presented at the Theobald Smith Society, Rutgers University.